December 2020

The Role of Grain Boundaries in the Tensile Deformation Behavior of CoCrFeMnNi High Entropy Alloys

Hyunsoo Lee
Clemson University, hyunsol@g.clemson.edu

The Role of Grain Boundaries in the Tensile Deformation Behavior of CoCrFeMnNi High Entropy Alloys

---

A Dissertation
Presented to
the Graduate School of
Clemson University

In Partial Fulfillment
of the Requirements for the Degree
Masters of Science
Mechanical Engineering

---

by
Hyunsoo Lee
Dec 2020

Accepted by:
Dr. Fadi F. Abdeljawad, Committee Chair
Dr. Huijuan Zhao
Dr. Garrett Pataky
Dr. Marian Kennedy

Abstract

High Entropy alloys (HEAs) are metal alloys consisting of multiple base metals in equimolar or near equimolar concentrations. HEAs exhibit unique combinations of properties that render them an attractive choice in many engineering applications. Among HEAs, a single phase face centered cubic (FCC) CoCrFeMnNi alloy, known as the Cantor alloy, shows simultaneous strength and ductility specifically at cryogenic temperatures. This has been attributed to the activation of deformation twinning as an additional mode of plastic deformation. Experimentally it has been observed that grain boundaries (GBs) facilitate the nucleation of deformation twins in HEAs. However, the role of GB geometry in the deformation behavior of HEAs remains unexplored. In this thesis work, we leverage atomistic simulations to systematically investigate the role of GB geometry in the deformation behavior of the Cantor alloy at 77 K. To this end, a series of Cantor alloy bicrystals with $\langle 110 \rangle$ and $\langle 111 \rangle$ symmetric twist GBs are constructed and used in tensile deformation simulations. Simulation results reveal that plastic deformation proceeds by the nucleation of partial dislocations from GBs, which then grow with further loading by bowing into the bulk crystals leaving behind stacking faults. Variations in the nucleation stress exist as function of GB character, defined in this work by the twist angle. Our results provide future avenues to explore GBs as a microstructure design tool to develop HEAs with tailored mechanical properties.

Acknowledgments

The research would not have been possible without the financial and emotional support of my advisor, Dr. Fadi F. Abdeljawad. The vast amount of his knowledge and attention to detail has been inspirational and kept my progress on track throughout this program. This research is also received great amount of help from the research team, FRAME, lead by Dr. Garrett Pataky. Mitra Shabanisamghabady, a Ph.D. candidate from Clemson University, has looked over my transcripts and answered, with patience, my numerous questions. This team provided us with invaluable information on the research subject, the Cantor alloy and continuously exchanged knowledge. I would also like to express my gratitude to my other committee members, Dr Huijan Zhao and Dr. Marian Molly Kennedy, for providing insightful comments to this research. My colleagues Maher Alghalayini, Malek Alkayyali, Omar Hussein, Thomas Lakas, and Yasir Mahmood saved me from a lot of errors and gladly gave up their weekends for my practice presentations. Learning programming and atomistic simulation from ground up was a great challenge for. The hard working culture of my research laboratory, Mat_2sim, always motivated me to keep the research on the right track as well. All the academic interaction with my colleagues greatly shorten the amount of time it took for me to familiarize with the tools required for the research.

Table of Contents

Title Page . . . . . **i**

Abstract . . . . . **ii**

Acknowledgments . . . . . **iii**

List of Tables . . . . . **vi**

List of Figures . . . . . **vii**

1 Introduction to High Entropy Alloys **1**
1.1 A Brief Historical Sketch 1
1.2 Thermodynamics of HEAs 2
1.3 Terminology 4
1.4 Four Core Effects 6
1.5 Development of HEAs 10

2 The Cantor Alloy **11**
2.1 The FCC CoCrFeMnNi (Cantor) 11
2.2 Mechanical Behavior of the Cantor Alloy 12

3 Open Questions and Research Plan **14**
3.1 Motivation 14
3.2 Open Research Questions 15
3.3 Research Plan 15

4 Method and Computational Approach **17**
4.1 GB Characterization 17
4.2 Coincidence-Site Lattice (CSL) 18
4.3 Preparation of GB Structures 19

5 Results and Discussion **23**
5.1 Twist GB Structures 23
5.2 Mechanical Deformation Behavior 25
5.3 Deformation Mechanisms 29
5.4 Strain Rate Effects 33
5.5 Multiple GBs 35
5.6 Effect of Chemical Disorder 37

6 Conclusions and Future Work **39**

Appendices **41**

A ⟨110⟩ GBs : Defect Nucleation 42
B ⟨111⟩ GBs : Defect Nucleation 43

Bibliography 44

List of Tables

1.1 Ideal configurational entropies in terms of the gas constant for equiatomic alloys with components up to 13 4
1.2 Configurational entropies calculated for conventional alloys at their liquid state . . . 6

4.1 Systematic GB categorization proposed by Wolf and Lutsko 18
4.2 For the bicrystal geometry depicted in Fig. 4.3(a), the crystal x-axis for the upper x_1 and lower x_2 crystals. The crystal z-axis is obtained using $\mathbf{z} = \mathbf{x} \times \mathbf{y}$, where the GB plane normal is along the crystal y-axis. The x-axis for single crystal systems with a [110] (SC_{110}) and [111] (SC_{111}) loading axis is also listed. 22

5.1 Tensile properties of the bicrystal with a Σ111 [111] GB at different strain rates . . . 33
5.2 Dimensions of the simulation box for the bicrystal systems with a Σ111 [111] GB with different numbers of GBs. 35

List of Figures

1.1 A schematic description of mixing process in the alloy system containing elements A and B . . . 2
1.2 A Molar free energy diagram. Variation of the free energy before mixing, G_1, as a function of the mole fraction of B component is depicted . . . 3
1.3 The change of free energy of mixing as function of composition and temperature for an ideal solution . . . 4
1.4 Categorization of HEAs based on configurational entropy . . . 5
1.5 Possible mixing reactions that can occur with three different prime elements. . . . 6
1.6 (a) Depiction of the lattice structure made of atoms with the radii of r_i and r_j. $\bar{r}$ in figure (b) represents the average radius of the atoms . . . 7
1.7 (a) Schematic representation of intrinsic lattice distortion effects on Bragg diffraction (b) distorted lattice with solid solutions of different atom sizes . . . 7
1.8 Temperature and distortion effects on x-ray diffraction intensity . . . 8
1.9 Hardness and lattice constants of $CuCoNiCrAl_xFe$ alloy system are plotted as a function of Al content, x. (A) hardness of $CuCoNiCrAl_xFe$ alloys, (B) lattice constants of an FCC phase, (C) lattice constants of a BCC phase . . . 9
1.10 Hardness for HEAs are compared with the conventional alloys including 17-4 PH stainless steel, Hastealloy, and 316 stainless steel . . . 9
1.11 Yield strength and density property space chart. Newly discovered HEAs are superimposed on the chart with the conventional alloys. The dashed lines give performance indices for uniaxial loading (slope, s=1), beam bending (s=3/2) and panel bending (s=2). The chart was made with the CES EduPack database, level 3 aerospace editio 10

2.1 Ashby plot of strength (σ_y) versus fracture toughness (K_c) for a wide range of materials including HEAs. The Cantor alloy has been shown to have a fracture toughness in the range 200-300 $MPa\sqrt{m}$, indicating that the alloy is among the most damage-tolerant materials . . . 12
2.2 The images show crystal structure of twinned grain in atomic scale . . . 13
2.3 Visual representation of dislocation dissociation and formation of stacking fault . . . 13

3.1 (a) A bright-field TEM image depicting nanotwin nucleation from a GB in a CoCrFeMnNi HEA at a true tensile strain $\epsilon = 12.1\%$ and temperature of 77 K. (b) EBSD image of deformation twins at room temperature. . . . 14
3.2 Investigation of the GB effect is limited to twist GBs. Two distinct twist axes and various misorientation angles for each axis were the main focus . . . 16

4.1 Variables that define a GB. x_A, y_A, z_A and x_B, y_B, z_B are the axes of the coordinates parallel to crystallographic directions in grains A and B, respectively. Here $\mathbf{o}$ and θ are the rotation axis and the rotation angle necessary to transfer both grains to an identical position. $\mathbf{n}$ denote the GB plane normal; it determines the orientation of the GB plane . . . 18

4.2 A top view of along the [001] direction on two interpenetrating cubic lattices misoriented by 22.6°. The dotted square area forms superlattice of coincident sites and represent Σ13 GB. 19
4.3 A schematic depicting (a) the geometry of the atomistic bi-crystal system and (b) the mechanical loading applied to these systems. 20
4.4 (a) 111 Zone axis (b) 110 Zone axis 21
4.5 Schematic description of STGB rotation. Each upper and lower crystal is misoriented by an equal and opposite angle $\theta/2$ relative to the reference axis 22

5.1 View of the GB plane showing the structure for select (a)-(c) [111] and (d)-(e) [110] STGBs. The structure of (a) Σ111, (b) Σ7, (c) Σ39, (d) Σ9, and (e) Σ17 STGBs are shown. Atoms are colored according to the centrosymmetry parameter, where lighter colors indicate greater deviation from local FCC ordering. For the Σ111 [111] STGB in (a), interfacial dislocation network (green) extracted using DXA are shown. 24
5.2 For the Cantor alloy bicrystals, [(a) and (c)] tensile stress-strain curves and [(b) and (d)] close-up views around the peak points. Curves for bicrystals with [(a) and (b)] [110] and [(c) and (d)] [111] STGBs are shown. Curves for Cantor alloy single crystals with [110] (SC_{110}) and [111] (SC_{111}) loading axis are shown for comparison. 26
5.3 High entropy alloy single crystal study, shows similar anisotropy 26
5.4 For the bicrystal with a Σ9 [110] STGB: (a) a schematic representation showing the GB plane (blue) and {111} plane (green); and (b)-(d) views along the normal to the {111} plane depicting the nucleation and growth of a 1/6 ⟨112⟩ dislocation at a nominal strain of (b) $\epsilon = 5.0\%$, (c) $\epsilon = 5.4\%$, and (d) $\epsilon = 5.5\%$. In (b)-(d), the black line represents the partial dislocation that demarcates regions of FCC (green) from HCP (red) atoms. The shaded region in blue denotes the intersection region of the GB and {111} planes. 27
5.5 Snapshots of the bicrystal with Σ111 [111] STGB at a nominal tensile strain of (a) $\epsilon = 6.1\%$, (b) $\epsilon = 6.2\%$, and (c) $\epsilon = 6.3\%$ depicting the initial stages of 1/6 ⟨112⟩ dislocation (green line) nucleation from the GB leaving behind a stacking fault (atoms in red). The orange lines represent the GB dislocation network and atoms in only one half of the bicrystal system are shown in blue for a better visualization of the defect structures. 28
5.6 For the bicrystals with [110] STGBs: (a)–(c) A comparison of the deformation behavior for the systems with (a) Σ3, (b) Σ9, and (c) Σ19 GBs at a nominal strain of $\epsilon = 6.3\%$, where red (blue) denote stacking faults (GB) atoms. Atoms with FCC ordering are removed for a better visualization of the structures. (d)–(f) At a nominal strain $\epsilon = 15\%$, close-up views depicting nano-twinning in [110] bicrystals with (d) Σ3, (e) Σ9, and (f) Σ19 STGBs, where atoms in green (red) denote FCC (HCP) ordering. 30
5.7 Evolution of the fraction of stacking fault atoms with respect to the total in each system as a function of tensile strain for bicrystal systems with a (a) [110] and (b) [111] loading axis. Stacking fault atoms were identified using the PTM algorithm . . 30
5.8 experimental result of twin volume fraction 31
5.9 For the bicrystals with [(a)–(b)] [110] and [(c)–(d)] [111] STGBs, plots of the ultimate [(a)–(c)] stress and [(b)–(d)] strain as a function of the GBs present in these systems. Ultimate stress and strain values for Cantor alloy single crystals (dashed red lines) are also plotted for comparison. 32
5.10 Stress–strain curves for Σ111 [111] STGB bi-crystal structures with various strain rates. 34
5.11 CoCrFeMnNi Cantor alloy stress-strain curves 34

5.12 Snapshots of the Σ111 [111] STGB bicrystals with different strain rates. (a) $\dot{\epsilon} = 4.8e{+}07$ $[s^{-1}]$ with the nucleation at $\epsilon = 5.90$ % (b) $\dot{\epsilon} = 1.6e{+}08$ $[s^{-1}]$ with the nucleation at $\epsilon = 6.03$ % (c) $\dot{\epsilon} = 4.8e{+}08$ $[s^{-1}]$ with the nucleation at $\epsilon = 6.40$ % (d) $\dot{\epsilon} = 1.4e{+}09$ $[s^{-1}]$ with the nucleation at $\epsilon = 7.20$ %(e) $\dot{\epsilon} = 4.8e{+}09$ $[s^{-1}]$ with the nucleation at $\epsilon = 8.62$ % 35
5.13 Cantor alloy bicrystals with multiple GBs. Atoms in green (white) denote FCC (GB) atoms, while atoms in orange denote rigid (left) and moving ones (right). 36
5.14 For the bicrystal system with a Σ111 GB, the onset of dislocation nucleation from the GB in a system with (a) one GB at a nominal strain of $\epsilon = 6.5$ % and (b) 15 GBs at a nominal strain of $\epsilon = 5.7$ %. 36
5.15 (a) Stress strain curves for the bicrystal system with a Σ111 GB with a varying number of GBs. (b) A close-up view around the peak points in the stress strain curves. 37
5.16 (a) Stress strain curves for five realizations of the bicrystal system with a Σ3 [111] GB, demonstrating the effect of local GB chemistry. The behavior of the single crystal with [111] loading axis is also shown for comparison. (b) Structure of one bicrystal system with a Σ3 [111] GB, showing the nucleation of a partial dislocation (green line) from the bulk crystal, which then leaves behind a stacking fault (atoms colored in red). GB atoms are in yellow and bulk FCC atoms were removed for a better visualization of the defect structures. 38

1 The FCC atoms located in either upper or lower crystal are deleted for visualization. One of crystals is chosen for deletion depending on the initial defect nucleation site. Blue spheres and red spheres represent FCC and HCP structure for each. The green lines wrap around HCP structure (stacking fault) and indicate partial dislocation lines. (a) Σ3 (b) Σ9 (c) Σ17 (d) Σ19 (e) Σ27 (f) Σ33 (g) Σ41 (h) Σ43 (i) Σ51 (j) Σ201 42
2 The FCC atoms located in either upper or lower crystal are deleted for visualization. One of crystals is chosen for deletion depending on the initial defect nucleation site. Blue spheres and red spheres represent FCC and HCP structure for each. The green lines wrap around HCP structure (stacking fault) and indicate partial dislocation lines. (a) Σ3 (b) Σ7 (c) Σ13 (d) Σ19 (e) Σ21 (f) Σ31 (g) Σ39 (h) Σ57 (i) Σ93 (j) Σ111 43

Chapter 1

Introduction to High Entropy Alloys

1.1 A Brief Historical Sketch

In traditional metallurgy, metallic alloys are synthesized and fabricated by introducing solute atoms (i.e., alloying elements) to the host material. These alloying elements greatly influence many of the physical and mechanical properties of structural and functional metals [1]. Notable examples of such an approach includes stainless steels and nickel-based alloys. In recent years, a new approach of fabricating metallic alloys has been introduced by using multiple elements in comparatively high concentrations, and such systems are termed high entropy alloys (HEAs). The first reported work on HEAs was introduced in 2002 by B. Cantor at the RQ11 conference in Oxford, and then officially published in 2004 [2]. Similar research published by S. Ranganathan discussed alloys which are closely related to HEAs and called the created alloys multimaterial cocktails [3]. Then, the term for alloys, HEAs, was used for the first time in the research published by Yeh et al. [4]. The name, HEAs, still remains as the convention to describe such alloys [4]. Owing to their multi-principal element compositions, HEAs are characterized by unique combinations of properties, including mechanical strength [4–6], hardness [7, 8], wear resistance [9, 10], and corrosion resistance [11–14]. The use of multiple principal elements in far-from dilute concentrations unlocks myriad possibilities of combinations of properties and functionalities that are not typically obtained in conventional metallic alloys.

1.2 Thermodynamics of HEAs

In order to provide context for HEA terminology, which is described in the next section, alloy thermodynamics is briefly introduced in this section. In a system composed of a single component, the equilibrium phase of the system is dependent on pressure and temperature. An alloy system, however, involves composition as an additional variable. For example, consider the simple binary solution system containing pure elements A and B as shown in Fig.1.1. The total Gibbs free energy of a binary solution can be calculated from the free energies of pure A and B element. Under the assumption that both the A and B have the same crystal structures and can be mixed in any proportions to make a solid solution with the same crystal structure, 1 mol of homogeneous solid solution is made by mixing together the mole fractions of A and B in the alloy. Mathematically, it can be expressed as

$$X_A + X_B = 1 \tag{1.1}$$

where X_A and X_B are the mole fractions of each component.

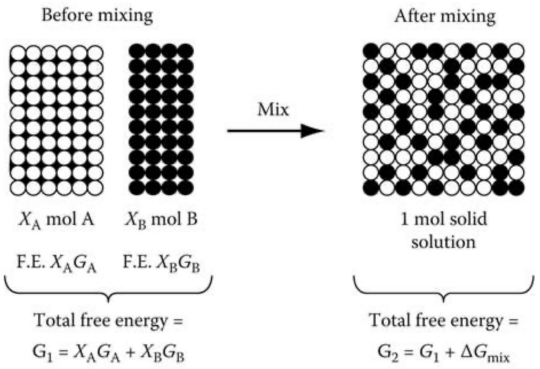

Figure 1.1: A schematic description of mixing process in the alloy system containing elements A and B [15].

Fig. 1.1 portrays the process that the A and B atoms are mixed together to make a homogeneous solid solution. The left image on the Fig. 1.1 shows the configuration of the system which has a Gibbs free energy, G_1, before mixing. G_1 lies on the straight line connecting the points that represent the free energies of pure A and pure B, refer to Fig. 1.2. After the mixing process, the free energy of the system changes to become

$$G_2 = G_1 + \Delta G_{mix} \tag{1.2}$$

G_2 is the total free energy after mixing and ΔG_{mix} is the change in energy caused by mixing.

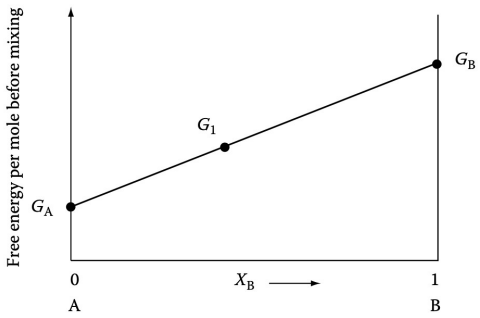

Figure 1.2: A Molar free energy diagram. Variation of the free energy before mixing, G_1, as a function of the mole fraction of B component is depicted [15].

The ΔG_{mix}, by the definition, can be divided into enthalpy (ΔH_{mix}) and entropy (ΔS_{mix}) change and is given by

$$\Delta G_{mix} = \Delta H_{mix} - T\Delta S_{mix} \tag{1.3}$$

For the sake of illustrating the concept of entropy of HEAs, we consider ideal alloys with $\Delta H_{mix} = 0$. In this case, the free energy change on mixing is only due to the change in entropy:

$$\Delta G_{mix} = -T\Delta S_{mix} \tag{1.4}$$

Thermal entropy can be quantified by invoking Boltzmann equation from statistical thermodynamics, which relates entropy to the possible configurations:

$$S = k\ ln\ \omega \tag{1.5}$$

where k is Boltzmann's constant and ω is a measure of randomness. In other words, ω is the number of possible arrangement of the atoms in the solution under the assumption that there is no change in volume and heat. In this binary solution system, when A and B mix to form a substitutional solid solution and all configurations of A and B are equally probable, the number of possible ways of arranging the atoms on the lattice sites can be expressed as the following:

$$\omega_{config} = \frac{(N_A + N_B)!}{N_A!N_B!} \tag{1.6}$$

Using Stirling's approximation ($\ln N! \approx N\ln N - N$), the mixing entropy is given by the following:

$$\Delta S_{mix} = -R(X_A lnX_A + X_B lnX_B), \tag{1.7}$$

where R is the gas constant. By substituting the entropy in the free energy of mixing, ΔG_{mix}, can be simplified as

$$\Delta G_{mix} = RT(X_A lnX_A + X_B lnX_B) \tag{1.8}$$

Fig. 1.3 shows a plot of ΔG_{mix}. The free energy change of mixing for an ideal solution decreases as X_B mol of B increases. The above analysis can be generalized to N number of components, leading

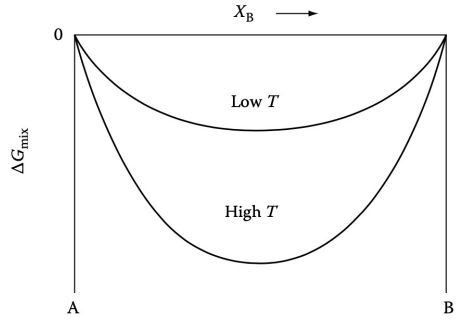

Figure 1.3: The change of free energy of mixing as function of composition and temperature for an ideal solution [15].

to entropy change as:

$$\Delta S_{mix} = -R(X_1 ln X_1 + X_2 ln X_2 + X_3 ln X_3 + ...) \tag{1.9}$$

From the above equation, we can see that the mixing entropy increases as the number of components in the system increases. Alloy thermodynamics of HEAs can be demonstrated by considering an equiatomic alloy with n number of components in regular solid state. Its ideal configuration entropy is calculated by [4, 16]

$$\Delta S_{conf} = -R(\frac{1}{n} ln \frac{1}{n} + \frac{1}{n} ln \frac{1}{n} + ... + \frac{1}{n} ln \frac{1}{n}) = -R\ ln\ \frac{1}{n} = R\ ln\ n \tag{1.10}$$

This is the configurational entropy calculated under the assumption that the atoms within the system are randomly arranged. Using the equation, we can easily compare the configurational entropy of systems with n number of components and this is illustrated in Table. 1.1.

Table 1.1: Ideal configurational entropies in terms of the gas constant for equiatomic alloys with components up to 13 [17]

n	1	2	3	4	5	6	7	8	9	10	11	12	13
$\Delta S_{conf}/R$	0	0.69	1.1	1.39	1.61	1.79	1.95	2.08	2.2	2.3	2.4	2.49	2.57

1.3 Terminology

Currently, two main schemes are used to define HEAs: an entropy-based or composition-based definitions. For the composition based definition, one of the early studies defined HEAs as "principal elements with the concentration of each element being between 35 and 5 at.%." [17] The definition is further expanded later on so that HEAs can contain minor elements [16]. For the second definition, entropy based definition uses the magnitude of the change of configurational entropy to

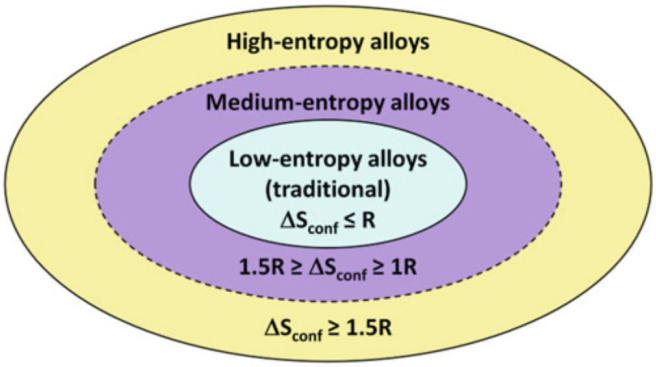

Figure 1.4: Categorization of HEAs based on configurational entropy [18].

categorize HEAs. In Fig. 1.4, each entropy category is graphically represented. As mentioned in the previous section, solid solutions with a high degree of randomness are easier to obtain as the number of components which have sufficient mole fraction in a system increases. Therefore, HEAs are defined as alloys having configurational entropies at a random state larger than 1.5R regardless of the phase state of the alloys at room temperature. This is expressed as the following equation:

$$\Delta S_{conf} \geq 1.5R \tag{1.11}$$

Medium-entropy alloys and low-entropy alloys are defined as the following [19]:

$$\text{Medium-entropy alloys} : 1.0R \leq \Delta S_{conf} \leq 1.5R \tag{1.12}$$

$$\text{low-entropy alloys} : \Delta S_{conf} \leq 1.0R \tag{1.13}$$

An entropy change of 1R sets the boundary between medium-entropy alloys and low-entropy alloys as a mixing entropy less than 1R is predicted to be much less competitive with the enthalpy of mixing. The reason that these boundaries need to be defined is that the basic design principle of HEAs is to have high mixing entropy so as to enhance the formation of random solid solution phases and hinder the formation of intermetallic compounds. For comparison, the configurational entropies of traditional alloys are listed in Table. 1.2.

Table 1.2: Configurational entropies calculated for conventional alloys at their liquid state [17]

Systems	Alloys	$\Delta S_{conf}/\mathrm{R}$ at liquid state
Low-alloy steel	4340	0.22, low entropy
Stainless steel	304	0.96, low entropy
	316	1.15, medium entropy
High-speed steel	M2	0.73, low entropy
Mg alloy	AZ91D	0.35 low entropy
Al alloy	2024	0.29, low entropy
	7075	0.43, low entropy
Cu alloy	7-3 brass	0.61, low entropy
Ni-based superalloy	Inconel 718	1.31, medium entropy
	Hastelloy X	1.37 medium entropy
Co-based superalloy	Stellite 6	1.13, medium entropy
Bulk metallic glass	$Cu_{47}Zr_{11}Ti_{34}Ni_8$	1.17, medium entropy
	$Zr_{53}Ti_5Cu_{16}Ni_{10}Al_{16}$	1.30, medium entropy

1.4 Four Core Effects

There are four core effects that distinguish HEAs from conventional alloys [3, 4, 17, 19] including the high entropy effect, the lattice distortion effect, sluggish diffusion, and the cocktail effect. The high entropy effect is first proposed by Yeh et al. [4]. It is hypothesized that the existence of multiple primary elements in near equiatomic concentration increases configurational entropy enough to overcome the enthalpies of compound formation such as intermetallic phases.

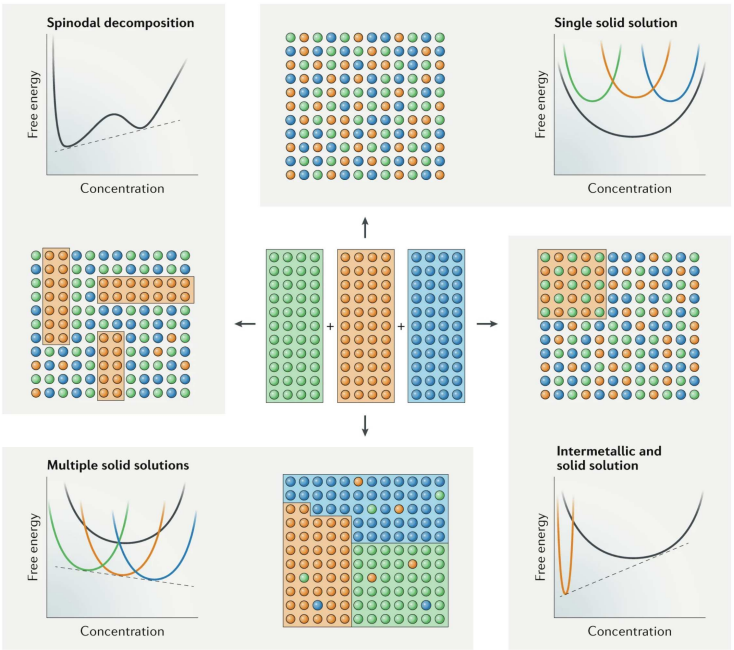

Figure 1.5: Possible mixing reactions that can occur with three different prime elements. [20]

To illustrate, the possible mixing of reactions of an alloy system with three alloying components are depicted graphically in Fig. 1.5. These include spinodal decomposition, solid solution, intermetallic formation, multiple solid solution. Spinodal decomposition is very commonly observed in HEAs [4, 21–25], including Fe-Ni-Mn [26, 27], Fe-Cr-Co [28] and Fe-Cr alloys [29]. In the mixing reaction that forms multiple solid solutions, each component in a system forms separate phases. Intermetallic compounds are undesirable as they make the alloy brittle [30–32]. Next, the lattice distortion effect states that the difference of atom sizes in solid solution distort lattice structure from ideal structure (Fig. 1.6).

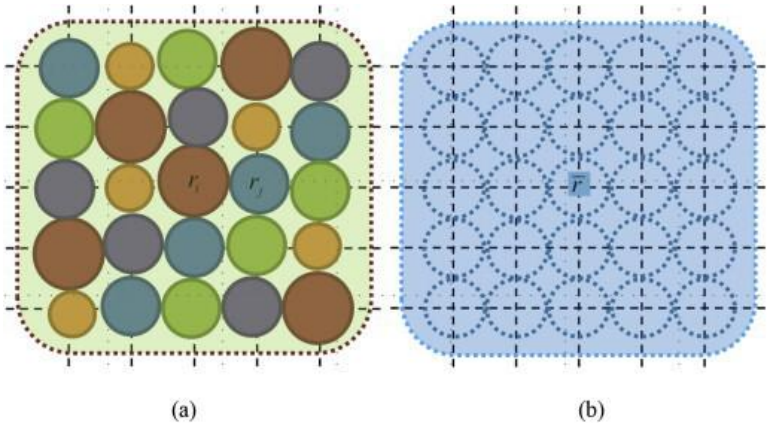

Figure 1.6: (a) Depiction of the lattice structure made of atoms with the radii of r_i and r_j. $\bar{r}$ in figure (b) represents the average radius of the atoms [33]

It is hypothesized that this effect has been demonstrated using the intensity of x-ray diffraction peaks [16, 34, 35]. The Fig. 1.7 shows the distortion effect on the x-ray diffraction graphically. When all atoms within the alloy system are placed in the perfect lattice sites, a beam of x-rays of

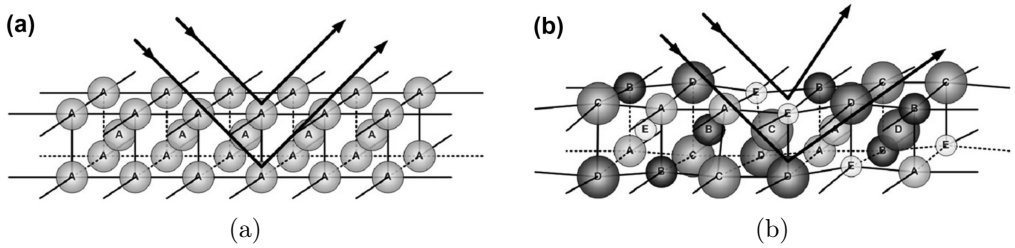

Figure 1.7: (a) Schematic representation of intrinsic lattice distortion effects on Bragg diffraction (b) distorted lattice with solid solutions of different atom sizes [33]

wavelength λ is incident on two parallel planes at an angle θ, creating sharp peaks on diffraction patterns due to constructive interference. However, the system composed of atoms with varying

atomic radii changes the diffraction angles, altering the interference pattern of the scattered rays. Hence, the lattice distortion effect decreases the x-ray diffraction intensities beyond the thermal effect as shown in Fig. 1.8. The lattice distortion effect has been shown to increase the hardness of

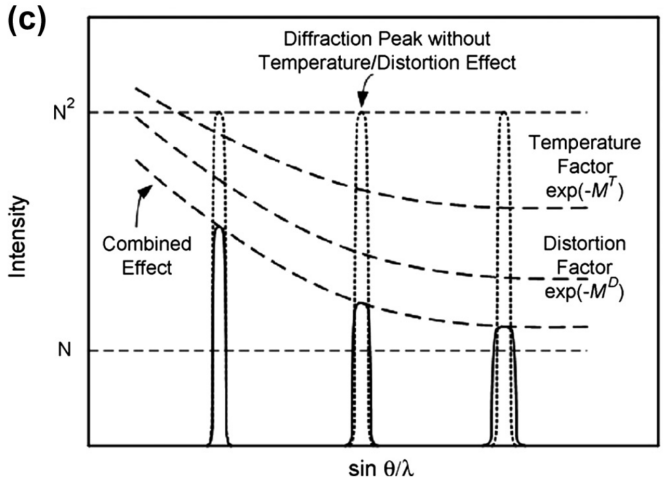

Figure 1.8: Temperature and distortion effects on x-ray diffraction intensity [36]

HEAs [16, 35]. Wang et al. [37] found a clear correlation between the magnitude of the local lattice distortion and the dislocation dissociation distance, showing the potential impact on deformation behavior on Cantor alloy. Li et al. [38] theoretically explored the effect of the lattice distortion and showed that the atomic mismatch brings solid solution strengthening effect. Zhao et al. [39] showed that the yield strength enhancement and lattice friction stress monotonically increase with increasing lattice mismatch strain. Additionally, the lattice distortion effect has been shown to be correlated with a decrease in electrical and thermal conductivities [16, 35]. The sluggish diffusion effect is proposed because diffusion is reported to be slow in HEAs [4]. As diffusion is hard to quantitatively measure, the hypothesis relies on indirect observations including the presence of nanocrystals in Al_xCoCrCuFeNi as-cast alloy [21] and AlCrMoSiTi after annealing [40]. However, Miracle et al. [41] analyzed HEA diffusion data and did not find clear evidence of slow kinetics in $CoCrFeMn_{0.5}Ni$.

The cocktail effect is used to indicate that the unexpected properties can be obtained from mixing many components. The cocktail effect was first demonstrated by Ranganathan [3] and the effect is confirmed by other studies [5, 6, 42–45]. The effect implies an increased flexibility in terms of tailoring the properties of HEAs. As an example, the hardness of $CoCrCuNiAl_x$ HEAs depending on the Al content is shown in Fig. 1.9; the hardness of the alloy increases with increasing Al content,

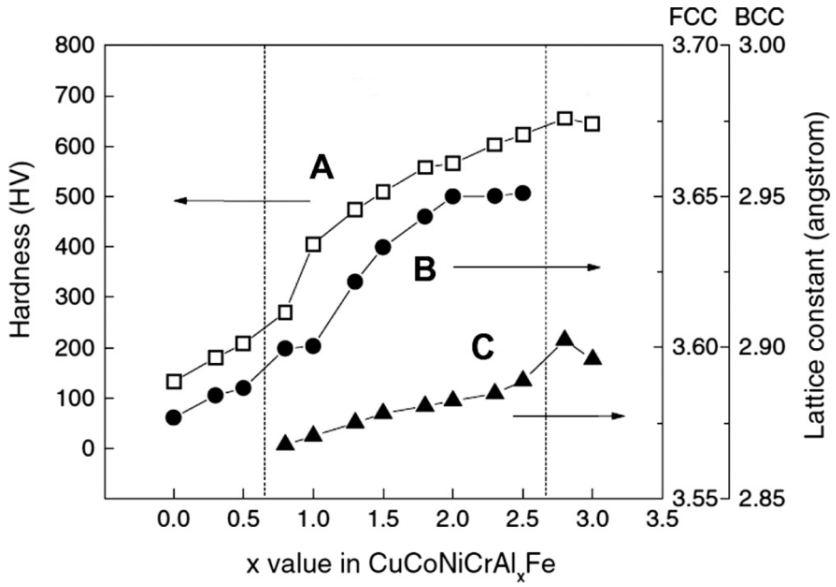

Figure 1.9: Hardness and lattice constants of CuCoNiCrAl$_x$Fe alloy system are plotted as a function of Al content, x. (A) hardness of CuCoNiCrAl$_x$Fe alloys, (B) lattice constants of an FCC phase, (C) lattice constants of a BCC phase [4].

implying that the characteristics of the alloy are customizable. To provide a general overview of the customizability of HEAs, the hardness of currently discovered HEAs is shown in Fig. 1.10, where it can be seen that the properties of HEAs can vary widely depending on the alloy content.

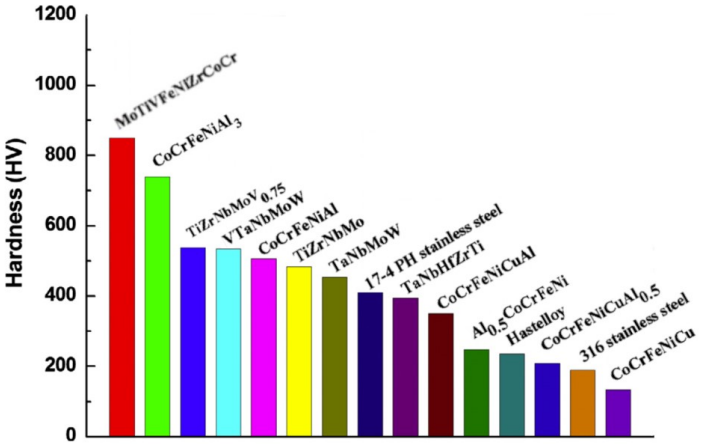

Figure 1.10: Hardness for HEAs are compared with the conventional alloys including 17-4 PH stainless steel, Hastealloy, and 316 stainless steel [46].

1.5 Development of HEAs

The multiple principal elements approach is revealing unexpected alloying mechanisms. Numerous recent studies on 3d transition metal HEAs, such as CoCrFeMnNi [2, 47–49], CoCrFeNi [47, 50], CoFeMnNi [47], CoCrMnNi [47], and $Co_{0.25}Cr_{0.1}Fe_2Mn_{1.35}Ni_{1.3}$ [51], have explored the impact of temperature [52, 53], grain size [54–56], alloy composition [57–59], strain rate [60], strain levels [61], and deformation-induced phase transformations [62, 63] on the mechanical behavior of these alloys. In addition, HEAs with new properties which fill the gaps in Ashby type maps are being discovered [64]. In Fig. 1.11, 3d transition and refractory metal HEAs fill a gap in the strength-density Ashby map between steels and Ti alloys. The continuous development of HEAs would provide designers with materials systems with unique combinations of properties.

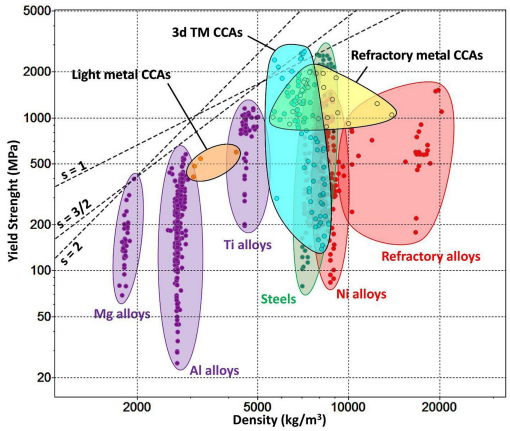

Figure 1.11: Yield strength and density property space chart. Newly discovered HEAs are superimposed on the chart with the conventional alloys. The dashed lines give performance indices for uniaxial loading (slope, s=1), beam bending (s=3/2) and panel bending (s=2). The chart was made with the CES EduPack database, level 3 aerospace edition by Gorsse et al. [64]

Chapter 2

The Cantor Alloy

2.1 The FCC CoCrFeMnNi (Cantor)

The Cantor alloy is a quinary alloy with CoCrFeMnNi composition. The alloy is one of the first HEAs to exist as a single FCC phase solid-solution [2]. The strength of this alloy is strongly temperature dependent below 473k and weakly at temperatures up to 1273K. In addition, modest strain-rate dependence was shown at low homologous temperatures [2]. Understanding the mechanical properties of the Cantor alloy has been the subject of active research efforts. Its elastic constants, determined using experimental [65, 66] and computational [67] techniques, were found to exhibit similar elastic anisotropy as Fe [68]. Experimental studies employed X-ray diffraction [69–73], scanning electron microscopy [70, 74–76], transmission electron microscopy [52], electron backscatter diffraction [75, 76], and atom probe tomography [77, 78] showed no indication of either short-range order, or clustering at a temperature over 800 K. However, a recent experimental study showed Cr rich precipitates and enrichment of Ni and Mn at the grain boundary (GB) below 1073 K [77] and suggested that entropy stabilizes the structure above 1073 K and lose over by enthalpy at below 1073 K. Further, density functional theory studies showed potential of phase transformation to hexagonal close-packed (HCP) below 50 K and two experimental studies implied pressure induced transition from FCC to HCP [62, 63].

2.2 Mechanical Behavior of the Cantor Alloy

The Cantor alloy was found to exhibit simultaneous mechanical strength and ductility [41, 48, 53, 54, 69, 79–84] with yield strength values that are comparable to conventional alloys, such as Ni-based superalloys and steels. A recent experimental study showed mechanical strength of 1 GPa and 60% elongation at cryogenic temperature, 77 K, and the work hardening rate increased as temperature decreased [52]. Gali and George [70] showed that the yield and ultimate strengths and ductility all increase simultaneously with decreasing temperature down to 77 K. The Cantor

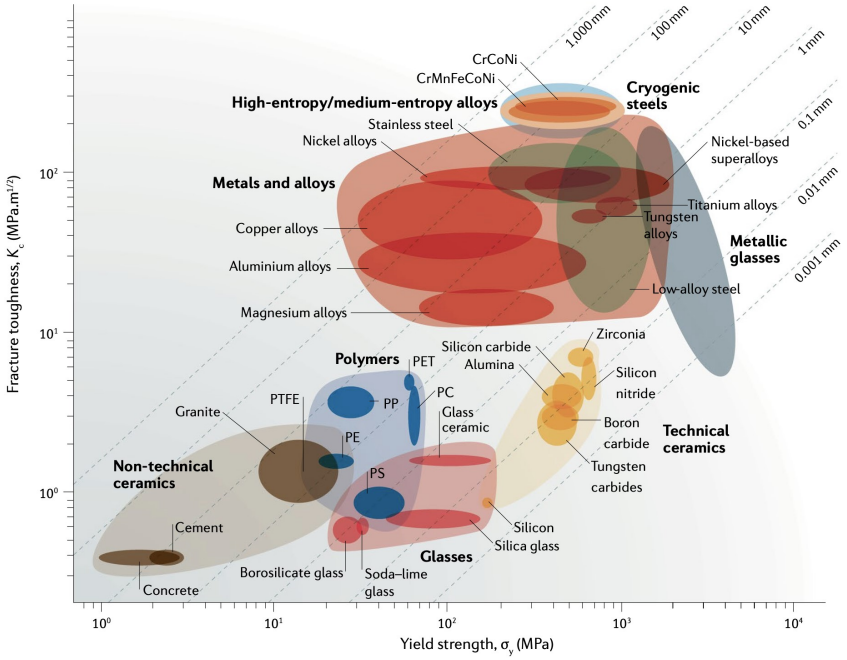

Figure 2.1: Ashby plot of strength (σ_y) versus fracture toughness (K_c) for a wide range of materials including HEAs. The Cantor alloy has been shown to have a fracture toughness in the range 200-300 $MPa\sqrt{m}$, indicating that the alloy is among the most damage-tolerant materials [20, 48].

alloy also showed higher damage tolerance than any known materials. Experimental results showed that the Cantor alloy has fracture toughness of over 200 MPa$\sqrt{m}$ [48, 52, 70], exceeding the fracture toughness of most pure metals and most metallic alloys. An Ashby plot of strength versus fracture toughness is presented in Fig. 2.1 and graphically represents the damage tolerance and the strength of the Cantor alloy compared to existing materials. The unique properties of the Cantor alloy are due to multiple deformation mechanisms. An experimental study at room temperature [52, 76, 85] observed the following deformation processes: slip initially occurs by planar glide $1/2\langle 110\rangle$ disloca-

tion on {111} plane and the emitted dislocations split into $1/6\langle 112\rangle$ Shockley partial dislocation. Deformation twinning is another mode of deformation that is observed in HEAs. As an illustration, the microstructure of a twinned crystal is visually represented in Fig. 2.2, where the twin planes are marked by arrows. It is evident that this process is not diffusive as atoms are only sheared by small distances, typically less than a lattice spacing. Extensive deformation-induced nanotwins have been observed in the Cantor alloy, as well as other FCC HEAs, at various temperatures, including 77 K, and with grain sizes ranging from sub-micrometer to millimeter [48, 52, 77, 79, 85, 86]. A $\langle 110\rangle$

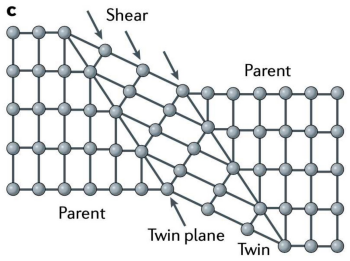

Figure 2.2: The images show crystal structure of twinned grain in atomic scale [20].

dislocation in an FCC lattice usually dissociates into two Shockley partials separated by a stacking fault defect as shown in Fig. 2.3. The distance between these two Shockley partials is referred to as the splitting distance. Generally speaking, the lower the stacking fault energy of a crystal, the larger the splitting distance between the partial dislocations and the wider stacking fault. Hence,

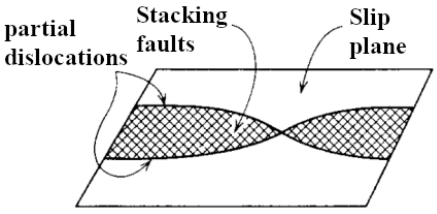

Figure 2.3: Visual representation of dislocation dissociation and formation of stacking fault [87].

the stacking fault energy provides useful insight into the deformation response of a metal. Otto et al. [52] showed that the extensive deformation twinning of the Cantor alloy at low temperatures is attributed to its low stacking fault energy. Atomistic calculations exploring the stacking fault energies in the Cantor alloy showed deformation twinning is thermodynamically favorable at low temperature [88, 89]. Further, experimental studies showed a relatively wide splitting distance of 3.5-4.5 nm with an average stacking fault energy of $30 \pm 5\ mJm^{-2}$ in the Cantor alloy [83, 85].

Chapter 3

Open Questions and Research Plan

3.1 Motivation

In terms of mechanical properties, the Cantor alloy has been shown to have high strength, ductility, and fracture toughness especially at low temperatures. Recent experimental studies revealed nanotwin nucleation from GBs [79, 83, 90], suggesting the role of GBs as twin nucleation sites. Fig. 3.1 (a) shows a bright-field TEM image from a study by Laplanche et al. [83] depicting the nucleation of deformation nanotwins from a GB in the Cantor alloy at a true tensile strain $\epsilon = 12.1\%$ and temperature of 77 K. Joo et al. [79] observed that deformation twins nucleated at GBs at room temperature as shown in Fig. 3.1 (b). The influence of GBs on twin nucleation has been observed previously in pure metals.

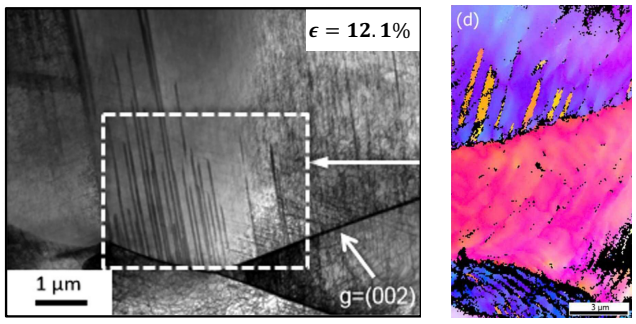

(a) (b)

Figure 3.1: (a) A bright-field TEM image depicting nanotwin nucleation from a GB in a CoCrFeMnNi HEA at a true tensile strain $\epsilon = 12.1\%$ and temperature of 77 K. Taken from Ref. [83]. (b) EBSD image of deformation twins at room temperature. Taken from Ref. [79]

The experiments by Bell and Cahn [91, 92] on Zn crystals highlighted the impact of defects on twin nucleation by observing that carefully prepared Zn single crystals can be mechanically loaded to much higher levels than those at which twins typically form in crystals with Mg-based [93, 94], and Ti-based [95, 96] systems. This carries implication for the development of the Cantor alloy with enhanced mechanical properties by designing HEA microstructures with desired density of GBs. A key step to achieving this goal is to gain an understanding of the role of GB type in defect nucleation in HEAs. The primary goal of this thesis work is to explore the role of GBs in the deformation mechanisms of equiatomic CoCrFeMnNi HEA. The ability to probe mechanisms controlling the unique properties of the Cantor alloy would improve our understanding of this new class of metallic alloys, enabling their use in many engineering application [46, 66].

3.2 Open Research Questions

While the Cantor alloy has been the subject of many investigations, the following research questions are still unanswered:

- Do GBs affect the nucleation process of deformation twins? The experimental evidence suggests that GBs may act as preferential sites for deformation twins nucleation [79, 83, 90].
- How does the GB geometry influence the defect nucleation stress? In general, a GB is defined by five geometric degrees of freedom; three for misorientation and two for plane normal [97].

3.3 Research Plan

In this work, we leveraged classical molecular dynamics to examine the role of GBs in the deformation behavior of the Cantor alloy. Especially, we focused our attention on the behavior at the cryogenic temperature. This is due to the fact that the alloy has shown extensive twinning at that temperature. Further, we explored the role of GB geometry in the defect nucleation stress in this alloy. We employed the coincidence lattice sites (CSL) to define and construct $\langle 110 \rangle$ and $\langle 111 \rangle$ symmetric twist GBs (STGBs). The reason for choosing twist GBs is two-fold. First, while the mechanical behavior of GBs has been the subject of active research in atomistic simulations, most studies have been mainly focused on tilt (symmetric or asymmetric) GBs. In such studies of tilt GBs, the angle of rotation about the tilt axis is varied leading to different GB types. However, this

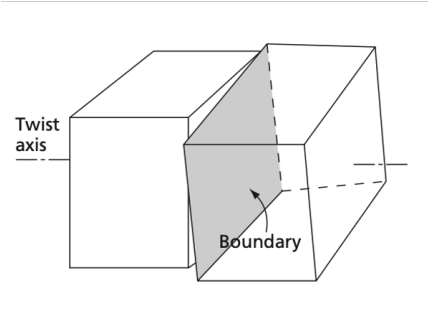

Figure 3.2: Investigation of the GB effect is limited to twist GBs. Two distinct twist axes and various misorientation angles for each axis were the main focus [1].

will result in bicrystal geometries with different crystal directions along the loading direction, leading to convoluted effects of GB type and resolved shear stresses on GB planes. Second, by using twist GBs we are able to probe the behavior of several GB types in bicrystal systems that all share the same loading axis and, thus, same maximum Schmid factors. In what follows, we briefly highlight the key steps in our atomistic simulation study.

- Generate a series of the Cantor alloy bicrystals with well defined GB geometry and perform thermal annealing at 77 K.
- Perform uniaxial tension on all bicrystal geometries up to 12% nominal strain at 77 K.
- Process and quantify the results by calculating the stress-strain curves and observing dislocation emission from GBs.

Chapter 4

Method and Computational Approach

4.1 GB Characterization

A GB is described by defining five geometric degrees of freedom (DOF); 3 for misorientation and 2 for plane normal: 2 DOF define the rotation axis (**o**), one defines the misorientation angle (θ), and two describe the GB plane normal (**n**). Fig. 4.1 schematically shows the GB plane normal and the rotation axis. The rotation axis can be described using Miller indices as $[h_0k_0l_0]$. The misorientation between two grains can then be described by the rotation axis and angle. The GB plane normal is described using Miller indices as $(h_{nA}k_{nA}l_{nA})$; the nA subscript denotes that the Miller indices are related to the grain A shown in Fig. 4.1. Using aforementioned parameters, any GB can be completely characterized by the notation $\theta^{\circ}[h_ok_ol_o],(h_{nA}k_{nA}l_{nA})$. Tilt GBs are defined as ones with a rotation axis, **o**, perpendicular to the GB normal. When the rotation axis and the GB normal are parallel to each other, the GBs are defined as twist GBs. Table. 4.1 shows one systematic way to categorize GBs. It is based on the GB plane described in both crystal 1 and crystal 2 coordinates, and the twist angle φ of both planes table.

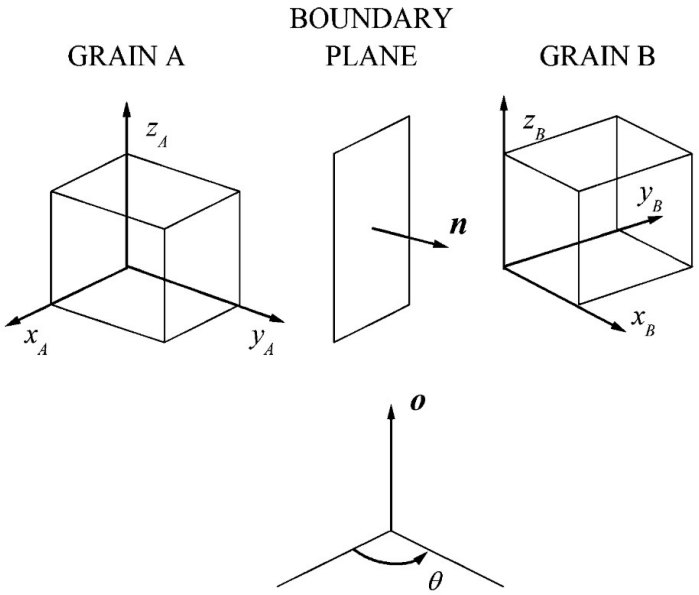

Figure 4.1: Variables that define a GB. x_A, y_A, z_A and x_B, y_B, z_B are the axes of the coordinates parallel to crystallographic directions in grains A and B, respectively. Here **o** and θ are the rotation axis and the rotation angle necessary to transfer both grains to an identical position. **n** denote the GB plane normal; it determines the orientation of the GB plane [97].

Table 4.1: Systematic GB categorization proposed by Wolf and Lutsko [97].

GB category	Standard
Symmetrical tilt GB	$h_1k_1l_1 = h_2k_2l_2$ *and* $\varphi = 0$
Asymmetrical tilt GB	$h_1k_1l_1 \neq h_2k_2l_2$ *and* $\varphi = 0$
Twist GB	$h_1k_1l_1 = h_2k_2l_2$ *and* $\varphi \neq 0$
Mixed GB	$h_1k_1l_1 \neq h_2k_2l_2$ *and* $\varphi \neq 0$

4.2 Coincidence-Site Lattice (CSL)

In this thesis, the CSL [98] model was used to describe the GBs used in this work. The concept is developed based on the assumption that the adjoining grains with a high number of atomic sites shared between the grains possess low interfacial energy because the number of broken bonds across the boundary is small. When the two grains are misoriented by a specified angle, θ, around a rotation axis, **o**, some atomic sites coincide at superposition of the two crystals, and these sites are termed coincidence sites. The coincidence sites form superlattice, and the parameter that characterizes the density of the coincident sites is Σ. The Σ value represents the reciprocal number

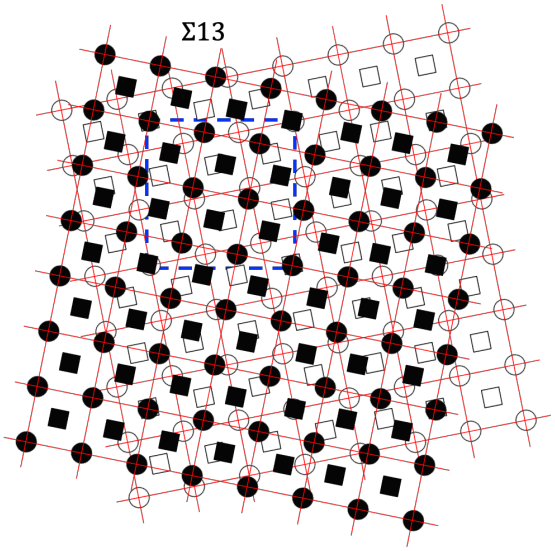

Figure 4.2: A top view of along the [001] direction on two interpenetrating cubic lattices misoriented by 22.6°. The dotted square area forms superlattice of coincident sites and represent Σ13 GB.

densities of lattice sites, and is given by:

$$\Sigma = \frac{\text{total number of lattice sites in elementary cell}}{\text{number of coincidence sites in an elementary cell}} \tag{4.1}$$

As an example, a two dimensional CSL GB is illustrated in Fig. 4.2 through a top view of two interpenetrating cubic crystal lattices denoted as filled and open markers. The crystals are rotated 22.6° relative to one another along their common [001] twist axis. The superimposed sites forming a superlattice, a CSL cell, are highlighted by a dotted blue square. This example shows that every thirteenth lattice site is the coincident site in 22.6° [001] misorientation relationship. The example boundary is Σ13.

4.3 Preparation of GB Structures

A series of the Cantor alloy bi-crystals with ⟨110⟩ and ⟨111⟩ STGBs were generated and studied using a second nearest-neighbor modified embedded atom method (MEAM) interatomic potential fit to the energetics of all unary, binary, and ternary combinations of the CoCrFeMnNi system [57]. This potential reproduces experimental mechanical properties and solid solution hardening effect in non-equiatomic CoCrFeMnNi HEAs at arbitrary compositions. All MD simulations reported here were performed using LAMMPS atomistic simulation package [99] and visualizations of atomistic structures were generated using OVITO [100]. Analysis of dislocation structures was

performed using the dislocation extraction algorithm (DXA) [101]. The OVITO implementation of the centrosymmetry parameter, common neighbor analysis (CNA), and polyhedral template matching (PTM) algorithm [102] were used to identify crystal structures and ordering in the atomistic systems.

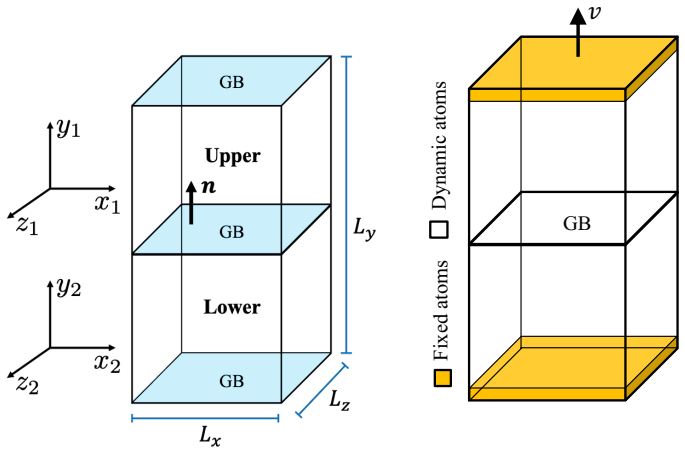

(a) (b)

Figure 4.3: A schematic depicting (a) the geometry of the atomistic bi-crystal system and (b) the mechanical loading applied to these systems.

The first step in our approach was the construction of Cantor alloy bicrystals with prescribed GB geometries. For each bi-crystal, a fully periodic atomistic system was created from two half crystals, each of which was rotated such that the resulting planar GB between the halves had the specified misorientation angle. Figure 4.3(a) shows a schematic representation of the bicrystal geometry used in this work, where the GB plane normal $\mathbf{n}$ aligns with the y-axis of both crystals, Table. 4.2 lists the ten [110] and ten [111] STGBs employed in our work in the order of increasing Σ value. Also included in the table are the twist angles, crystal x-axis for the upper (x_1) and lower (x_2) grains. Fig. 4.4 (a) and (b) show respectively the [111] and [110] zone axes, where several crystallographic directions are also identified. During the construction of the bicrystals, a sequence of relative displacements between the upper and lower half-crystals is used in conjunction with atom deletions and conjugate gradient energy minimizations to identify a low energy GB configuration. The systems were allowed to expand or contract in the perpendicular direction to the GB plane. In order to capture the periodicity of a GB atomic structure, the target dimensions of the bicrystal geometry were set to $L_x = L_z = 100$ Å and $L_y = 600$ Å. However, the dimension of each sample varied slightly so as to accommodate an integer number of unit cells necessary to model each specific

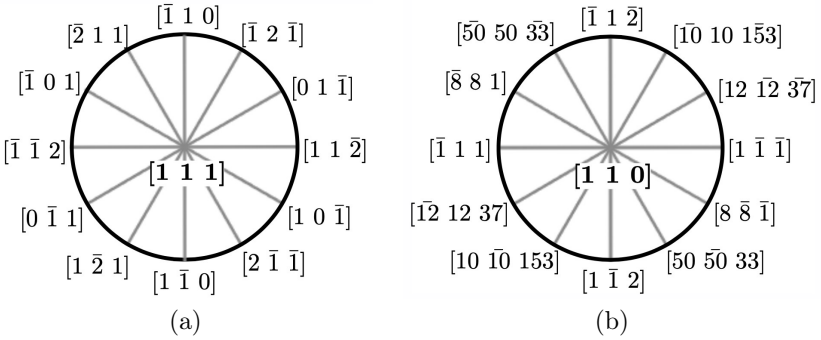

Figure 4.4: (a) 111 Zone axis (b) 110 Zone axis

GB. The number of atoms in each sample ranged from 600,000 to 1 million, and Ni, Fe, Mn, Cr, and Co atoms were randomly assigned in equal amounts. After the bi-crystal construction step, we thermally equilibrated the systems by heating the simulation box to a temperature of 77 K and holding for 4 ns with a target pressure of zero, allowing the system to expand or contract as appropriate. This was achieved by performing isothermal and isobaric integration with a 1 fs time step to march atoms' positions and velocities using a Nose-Hoover thermostat and barostat [103]. This creates a trajectory in phase space that is consistent with the isothermal-isobaric (NPT) ensemble. To damp undesirable oscillations in the system's temperature and pressure, the drag option within LAMMPS was used.

Table 4.2: For the bicrystal geometry depicted in Fig. 4.3(a), the crystal x-axis for the upper x_1 and lower x_2 crystals. The crystal z-axis is obtained using $\mathbf{z} = \mathbf{x} \times \mathbf{y}$, where the GB plane normal is along the crystal y-axis. The x-axis for single crystal systems with a [110] (SC_{110}) and [111] (SC_{111}) loading axis is also listed.

[110] STGBs			[111] STGBs		
Σ value	$\mathbf{x}_1$ / $\mathbf{x}_2$ $[hkl]_{upper}$ / $[hkl]_{lower}$	θ (°)	Σ value	$\mathbf{x}_1$ / $\mathbf{x}_2$ $[hkl]_{upper}$ / $[hkl]_{lower}$	θ (°)
3	$[1\ \bar{1}\ \bar{1}]$ / $[\bar{1}\ 1\ \bar{1}]$	70.53	3	$[1\ 1\ \bar{2}]$ / $[\bar{1}\ \bar{1}\ 2]$	60.00
9	$[2\ \bar{2}\ \bar{1}]$ / $[\bar{2}\ 2\ \bar{1}]$	38.95	7	$[1\ 4\ \bar{5}]$ / $[4\ 1\ \bar{5}]$	38.21
17	$[2\ \bar{2}\ \bar{3}]$ / $[\bar{2}\ 2\ \bar{3}]$	86.60	13	$[2\ 5\ \bar{7}]$ / $[5\ 2\ \bar{7}]$	27.80
19	$[3\ \bar{3}\ \bar{1}]$ / $[\bar{3}\ 3\ \bar{1}]$	26.53	19	$[1\ 7\ \bar{8}]$ / $[7\ 1\ \bar{8}]$	46.83
27	$[1\ \bar{1}\ \bar{5}]$ / $[\bar{1}\ 1\ \bar{5}]$	31.60	21	$[1\ 4\ \bar{5}]$ / $[\bar{1}\ 5\ \bar{4}]$	21.79
33	$[2\ \bar{2}\ \bar{5}]$ / $[\bar{2}\ 2\ \bar{5}]$	58.98	31	$[4\ 7\ \bar{11}]$ / $[7\ 4\ \bar{11}]$	17.90
41	$[4\ \bar{4}\ \bar{3}]$ / $[\bar{4}\ 4\ \bar{3}]$	55.88	39	$[2\ 5\ \bar{7}]$ / $[\bar{2}\ 7\ \bar{5}]$	32.20
43	$[3\ \bar{3}\ \bar{5}]$ / $[\bar{3}\ 3\ \bar{5}]$	80.63	57	$[1\ 7\ \bar{8}]$ / $[\bar{1}\ 8\ \bar{7}]$	13.17
51	$[5\ \bar{5}\ \bar{1}]$ / $[\bar{5}\ 5\ \bar{1}]$	16.10	93	$[4\ 7\ \bar{11}]$ / $[\bar{4}\ 11\ \bar{7}]$	42.10
201	$[10\ \bar{10}\ \bar{1}]$ / $[10\ \bar{10}\ 1]$	8.10	111	$[1\ 10\ \bar{11}]$ / $[\bar{1}\ 11\ \bar{10}]$	9.43
SC_{110}	$\mathbf{x} = [2\ \bar{2}\ \bar{5}]$	—	SC_{111}	$\mathbf{x} = [1\ 1\ \bar{2}]$	—

The GBs chosen for this study were $\langle 110 \rangle$ and $\langle 111 \rangle$ STGBs with a wide range of twist angles and, as a result, GB structures. Each of the two half crystals was rotated about the twist axis (i.e., the crystal y-axis given by [110] or [111]) by an equal and opposite angle $\theta/2$, where θ defines the total twist angle as described in Fig. 4.5. The x-direction for each of the crystals after the rotation is also shown in Table 4.2.

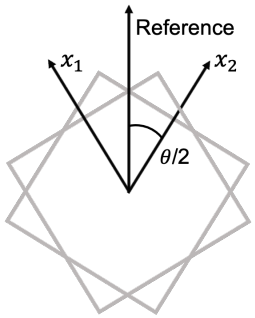

Figure 4.5: Schematic description of STGB rotation. Each upper and lower crystal is misoriented by an equal and opposite angle $\theta/2$ relative to the reference axis.

Chapter 5

Results and Discussion

5.1 Twist GB Structures

Projected views of the GB plane depicting the 0 K equilibrated structures before mechanical deformation for five selected GBs are shown in Fig. 5.1. Atoms are colored according to the centrosymmetry parameter, where the atoms with lighter shade indicate greater deviations from local FCC ordering. The atomic structures for the Σ111, Σ7, and Σ39 [111] GBs are shown in Fig. 5.1(a)–(c), respectively, whereas Fig. 5.1(d)–(e) shows Σ9 and Σ17 [110] GBs respectively. In Fig. 5.1(a) representing the structure of the Σ111 [111] STGB, DXA was used to reveal and characterize the interfacial dislocation network, shown in green lines, within the GB plane. For this low-twist angle GB, the boundary is comprised of a grid of $1/6$ $\langle 112 \rangle$ partial screw dislocations with alternating regions of FCC (atoms colored in black) and HCP (atoms colored in gray) structures, indicating faulted regions. Similar interfacial dislocation networks in low-angle twist GBs have been recently observed with atomistic calculations [104, 105]. Chen et al. [106] examined the GB character distribution in the Cantor alloy during recrystallization and showed a high density of twin Σ3 and low-angle GBs. In a recent study by Lin et al. [107], high-resolution microscopy was employed to study boundary dislocations at low-angle (≈ 6 °) GBs in the Cantor alloy and determine their Burgers vectors and dislocation spacing. Here, it is worth noting that while the GB generation algorithm used in this work resulted in equilibrated GB structures at 0 K by performing a series of rigid body translations within the GB plane, i.e., so-called γ-surface method [108, 109], chemical equilibration was not performed. Such a step includes probing the preferential sites with the GB

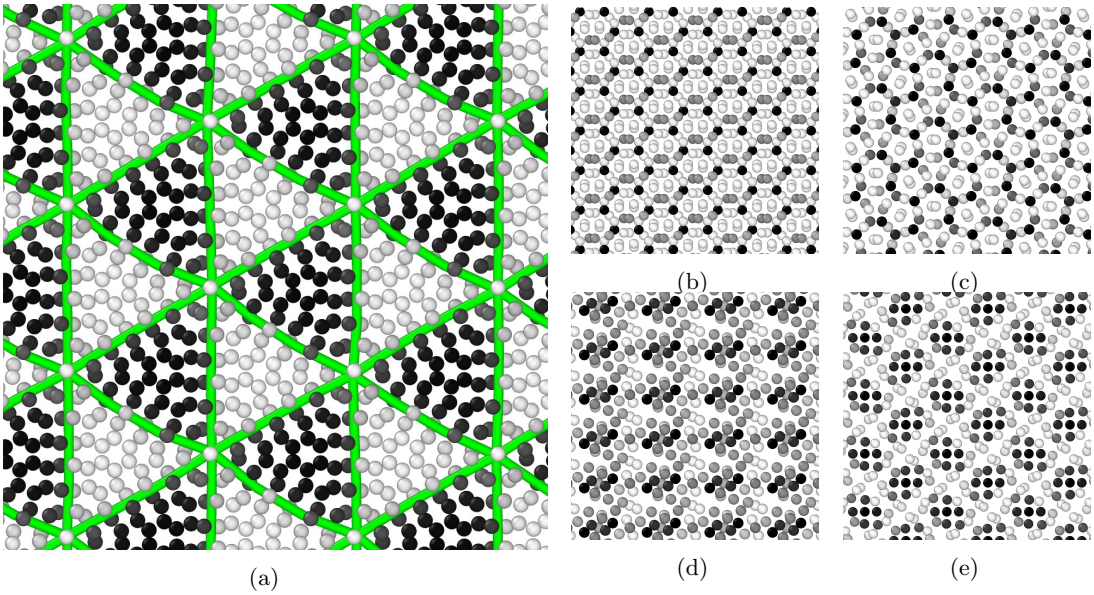

Figure 5.1: View of the GB plane showing the structure for select (a)-(c) [111] and (d)-(e) [110] STGBs. The structure of (a) Σ111, (b) Σ7, (c) Σ39, (d) Σ9, and (e) Σ17 STGBs are shown. Atoms are colored according to the centrosymmetry parameter, where lighter colors indicate greater deviation from local FCC ordering. For the Σ111 [111] STGB in (a), interfacial dislocation network (green) extracted using DXA are shown.

plane for each of the elemental species, sampling and optimizing the GB atomic density, and probing segregation effects of one or more elemental species to the GB. The phase space of possible chemical configurations for the equiatomic five-component Cantor system is large and beyond the scope of this thesis work. Very recently, Frolov et al. [110] and Zhu et al. [111] developed an evolutionary algorithm that performs a grand-canonical GB structure search and were able to identify a plethora of GB phases with different structures in pure metals. Also, Wynblatt and Chatain [112] in a recent computational study have shown using Monte Carlo, molecular dynamics, and lattice statics methods that both Cr and Mn segregate to GBs in the CoCrFeMnNi Cantor alloy. The study found that such segregation leads to depletion of bulk compositions when the grain size of these alloys is reduced into the nanoscale. As a result, the GB structures explored in this work can be regarded as metastable ones. Indeed, the multiplicity of metastable GB states has been the subject of active research recently for its influence on the behavior and properties of metallic systems [113, 114].

5.2 Mechanical Deformation Behavior

After the initial construction and thermal equilibration steps, uniaxial tension up to 12% was performed along the y-axis of each sample at 77 K and zero pressure in the transverse directions using the NPT ensemble. This was achieved by defining two slabs in which the atoms were fixed in their positions relative to each another; refer to Fig. 4.3(b) for a schematic representation of the mechanical deformation simulations. The slabs used to impose boundary conditions and forces on the dynamic atoms had a thickness of $\approx$ 25 Å. Uniaxial tension was applied by moving all fixed atoms of the upper slab with the same constant velocity of $v = 0.3$ Å/ps along the y-direction, while the lower slab remained fixed. The nominal strain along the y-direction of the sample was calculated as $\epsilon_{yy} = \Delta L_y / L_y(0)$, where $L_y(0)$ is the initial length, and the stress tensor averaged over all dynamic atoms was computed using the standard virial expression. We first start by examining the macroscopic mechanical behavior of the bicrystal systems at 77 K. Figure 5.2 shows stress-strain curves for the Cantor alloy bicrystals with [110] (Fig. 5.2(a)–(b)) and [111] (Fig. 5.2(c)–(d)) STGBs. The behavior of Cantor alloy single crystals with [110] (SC_{110}) and [111] (SC_{111}) loading axis are included for comparison. In all systems, the tensile stress increased monotonically with strain until a peak point was reached then followed by a stress drop, the value of which was roughly 35% of the peak value. It is also noticed that the peak point in the stress-strain curve in bicrystal systems was lower than their single crystal counterparts. As will be discussed later, these stress drops are associated with partial dislocation nucleation events with GBs serving as heterogeneous nucleation sites. An exception to this is the bicrystal system with $\Sigma 3$ (111) STGB, where a close examination of Fig. 5.2(c)–(d) shows that the peak stress for this system is comparable to the single crystal one. The coherent $\Sigma 3$ (111) STGB is resistant to nucleation of defects, which in this system were found to nucleate homogeneously from the bulk crystals. For the systems with a [110] loading axis, the maximum Schmid factor for $\{111\}\langle 112\rangle$ twinning is 0.47 and that for $\{111\}\langle 110\rangle$ slip is 0.41. However, for bicrystal geometries with a [111] loading axis those factors were 0.31 and 0.27 for twinning and slip, respectively. As a result, the [111] is the stiffer direction and bicrystals with a [111] loading axis attained higher stress states than those with a [110] loading axis.

An experimental study also observed sharp stress drop similar to our $\langle 111\rangle$ STGB. Kireeva et al. [115] conducted the tensile loading experiment with Cantor alloy single crystals. Each crystal showed different tensile loading response depending on its crystal orientation. On the $[\bar{1}11]$ crys-

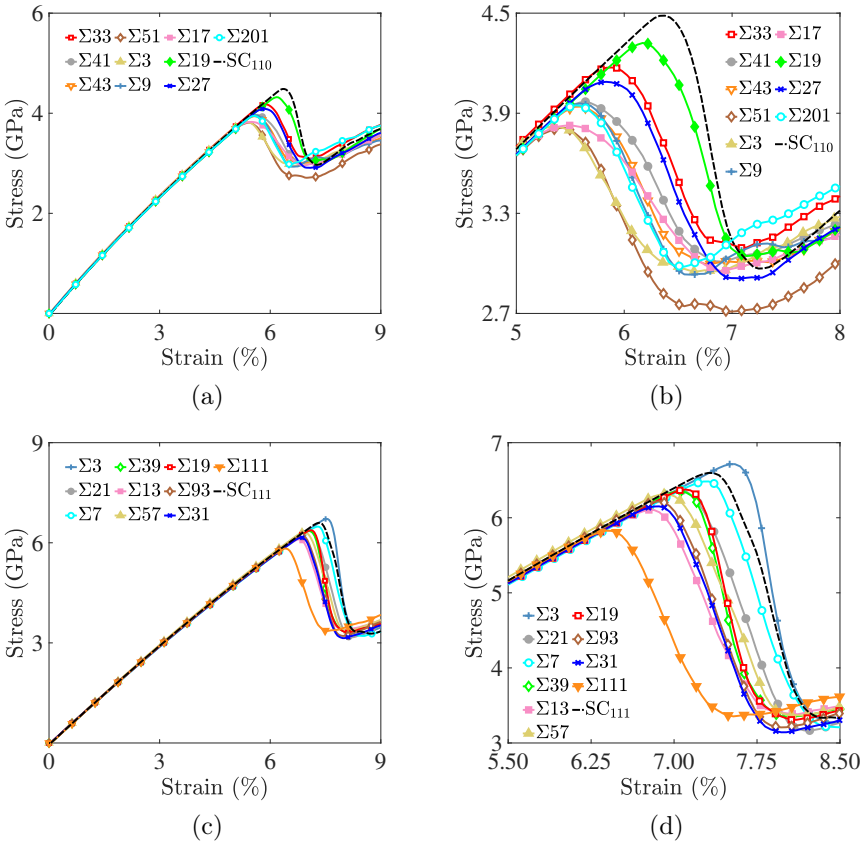

Figure 5.2: For the Cantor alloy bicrystals, [(a) and (c)] tensile stress-strain curves and [(b) and (d)] close-up views around the peak points. Curves for bicrystals with [(a) and (b)] [110] and [(c) and (d)] [111] STGBs are shown. Curves for Cantor alloy single crystals with [110] (SC_{110}) and [111] (SC_{111}) loading axis are shown for comparison.

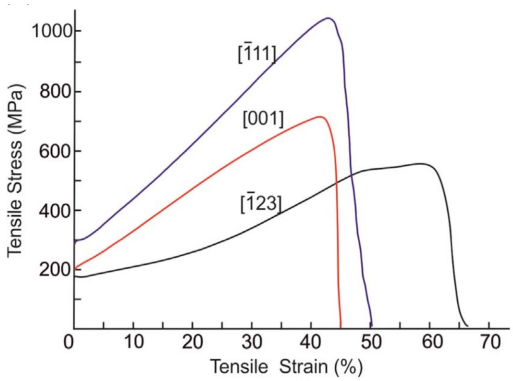

Figure 5.3: High entropy alloy single crystal study, shows similar anisotropy [115].

tal orientation, the crystal showed a sharp drop in the stress comparable to our ⟨111⟩ simulation Fig. 5.2(c) and (d). This sharp drop is due to the lower level of resolved shear stress on [111] loading direction compared to the [110] direction, allowing the crystal to achieve higher stress state before the emission of dislocations. Also, Fig. 5.2(a) and (c) shows that in all bicrystal systems explored in this work, a plateau in the stress was observed after the initial stress drops. As will be discussed below, this plateau in the flow stress is due to the fact that further deformation was achieved by the growth of GB-nucleated defects (i.e., dislocations) into the bulk grains. Similar trends for the flow stress have been observed in several metallic systems [116, 117]. Next, we visually inspect the atomic structures of the Cantor alloy bicrystals during the course of their tensile deformation with a specific focus at tensile strains near the peak points in the stress-strain diagrams. Here, the PTM algorithm was used to identify the local structural environment around each atom (FCC, HCP, etc.) and reveal GB regions and stacking faults that form during deformation. For example, Fig. 5.4 depicts results for the bicrystal system with a Σ9 [110] STGB, where Fig. 5.4(a) is a schematic illustrating the intersection of a {111} plane with this GB. Figure 5.4(b)–(d) shows respectively projected views normal to this {111} plane at nominal tensile strains $\epsilon = 5.0\%$, 5.4% and 5.5%, where the GB region is labeled in blue, FCC atoms in green, and HCP ones, indicative of stacking faults, in red. A 1/6 ⟨112⟩ partial dislocation line, identified by DXA and labeled in black, was observed to nucleate from the GB and propagate into the bulk crystal leaving behind a stacking fault. The nucleation of this partial dislocation corresponded to the stress drop observed for this bicrystal system [refer to Fig. 5.2(b)].

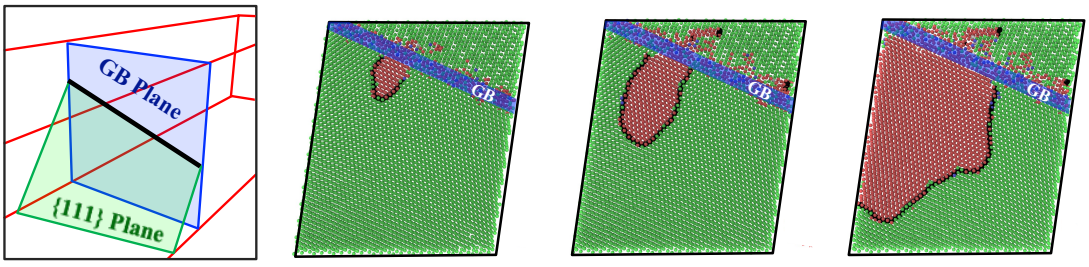

Figure 5.4: For the bicrystal with a Σ9 [110] STGB: (a) a schematic representation showing the GB plane (blue) and {111} plane (green); and (b)-(d) views along the normal to the {111} plane depicting the nucleation and growth of a 1/6 ⟨112⟩ dislocation at a nominal strain of (b) $\epsilon = 5.0\%$, (c) $\epsilon = 5.4\%$, and (d) $\epsilon = 5.5\%$. In (b)-(d), the black line represents the partial dislocation that demarcates regions of FCC (green) from HCP (red) atoms. The shaded region in blue denotes the intersection region of the GB and {111} planes.

Perspective views demonstrating the nucleation and growth of a partial dislocation in the bicrystal system with a $\Sigma 111$ [111] STGB are shown in Fig. 5.5. Snapshots at tensile strains $\epsilon = 6.1\%$ [Fig. 5.5(a)], 6.2% [Fig. 5.5(b)] and 6.3% [Fig. 5.5(c)] are shown, where the grid of GB dislocations is colored in orange, atoms in one crystal are colored in blue, and ones in the second crystal are removed for a better visualization of the defect structures. The nucleated dislocation line is colored in green and atoms with HCP structures are in red. At a tensile strain of $\epsilon = 6.1\%$, a $1/6\ \langle 112 \rangle$ partial dislocation line nucleated from the GB and grew by bowing out into the bulk crystal leaving behind a stacking fault. It is observed that the dislocation line has its ends pinned at two nodes of the GB dislocation network [see arrows in Fig. 5.5(a)]. Again, the stress drop observed in the stress-strain curve for this bicrystal system [refer to Fig. 5.2(d)] corresponded to the nucleation of this partial dislocation from the GB. As shown in Appendix A and B, all bicrystal systems examined in this work exhibited similar trends to the ones depicted in Figs. 5.4 and 5.5. Such results suggest that GBs serve as heterogeneous nucleation sites for dislocations in the Cantor alloy, and upon further straining these line defects grow into the bulk crystals leaving behind faulted regions. It is also observed that in all bicrystal systems explored in this work, no trailing partials were observed to nucleate from the GBs. This effect was also observed in atomistic simulations of dislocation nucleation from GBs in pure metals [117, 118]. Derlet and Van Swygenhoven [119] found that the emission of first partials was enough to relieve local stresses at GBs and that the emission of trailing partials was not necessary to accommodate the applied loading.

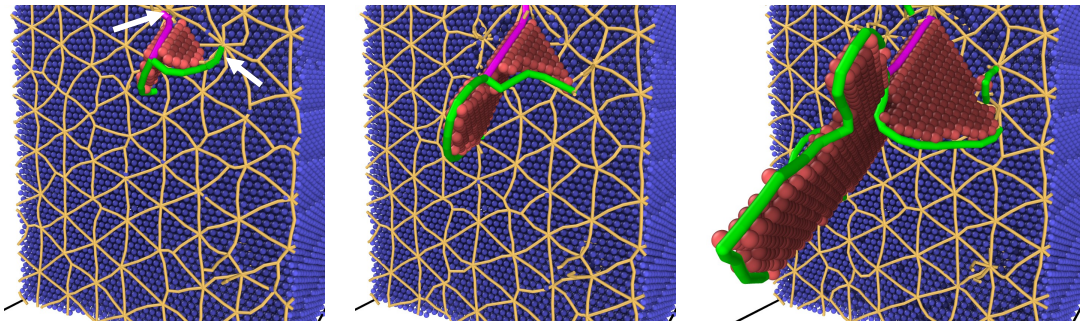

(a) (b) (c)

Figure 5.5: Snapshots of the bicrystal with $\Sigma 111$ [111] STGB at a nominal tensile strain of (a) $\epsilon = 6.1\%$, (b) $\epsilon = 6.2\%$, and (c) $\epsilon = 6.3\%$ depicting the initial stages of $1/6\ \langle 112 \rangle$ dislocation (green line) nucleation from the GB leaving behind a stacking fault (atoms in red). The orange lines represent the GB dislocation network and atoms in only one half of the bicrystal system are shown in blue for a better visualization of the defect structures.

5.3 Deformation Mechanisms

The mechanical behavior of the bicrystal systems is explored at late stages of deformation. Figure 5.6(a)-(c) shows respectively snapshots at a nominal tensile strain of $\epsilon = 6.3\%$ the bicrystals with $\Sigma3$, $\Sigma9$, and $\Sigma19$ [110] STGBs. In these figures, GB and HCP atoms were labeled in blue and red, respectively, where HCP ordering is indicative of stacking faults. Atoms with FCC structures were removed to provide a better visualization of the defect structures. As can be seen from Fig. 5.6, the density of the nucleated partial dislocations and the resultant stacking faults at a given strain are dependent on the GBs present in these systems. For example, the bicrystal with a $\Sigma9$ [110] STGB shown in Fig. 5.6(b) exhibits higher density of faulted regions compared to the one with a $\Sigma19$ [110] STGB depicted in Fig. 5.6(c). A close examination of the stress-strain curves for these bicrystals [refer to Fig. 5.2(b)] shows that the stress required to nucleate these partial dislocations was higher for the system with a $\Sigma19$ [110] STGB than ones with $\Sigma9$ and $\Sigma3$ [110] GBs. At a tensile strain $\epsilon = 15\%$, Fig. 5.6(d)–(f) shows, respectively, close-up views of the atomic structures for the bicrystals with a $\Sigma3$, $\Sigma9$ and $\Sigma19$ [110] STGBs, where deformation nano-twins can be observed in these systems. Here, atoms colored in green and red denote FCC and HCP structures. In all bicrystal systems examined in this thesis work, GBs were found to facilitate the nucleation of defects (i.e., dislocations). An exception to this is the bicrystal with the coherent $\Sigma3$ (111) STGB, where dislocations were found to nucleate homogeneously from the bulk crystals. This explains the large value of the peak stress for this system compared to the other bicrystal ones. Indeed, this effect has also been observed in other metallic systems [117].

Following the experimental approach by Laplanche et al. [83], we quantified the microstructural evolution during mechanical deformation by calculating the fraction of stacking fault atoms with respect to the total in each system, and the results are reported in Fig. 5.7 for bicrystals with a [110] (Fig. 5.7(a)) and [111] (Fig. 5.7(b)) loading axes. Stacking fault atoms were identified as ones with HCP ordering using the PTM algorithm. As mentioned above, the observed stress drop in the stress-strain diagrams corresponded to the nucleation of partial dislocations from GBs, which in turn grew rapidly into the bulk crystals leaving behind faulted regions. No stacking faults were observed to nucleate prior to reaching the peak point in the stress-strain diagram. In all bicrystal systems, the rapid increase in the fraction of faulted atoms at lower strain values compared to the single crystal systems indicates that GBs serve as efficient nucleation sites for partial dislocations.

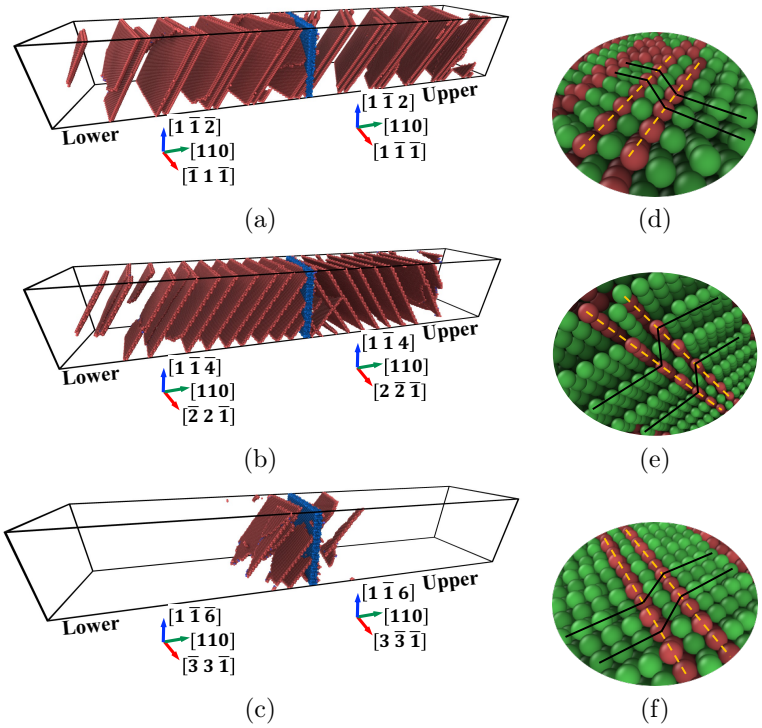

Figure 5.6: For the bicrystals with [110] STGBs: (a)–(c) A comparison of the deformation behavior for the systems with (a) Σ3, (b) Σ9, and (c) Σ19 GBs at a nominal strain of $\epsilon = 6.3\%$, where red (blue) denote stacking faults (GB) atoms. Atoms with FCC ordering are removed for a better visualization of the structures. (d)–(f) At a nominal strain $\epsilon = 15\%$, close-up views depicting nano-twinning in [110] bicrystals with (d) Σ3, (e) Σ9, and (f) Σ19 STGBs, where atoms in green (red) denote FCC (HCP) ordering.

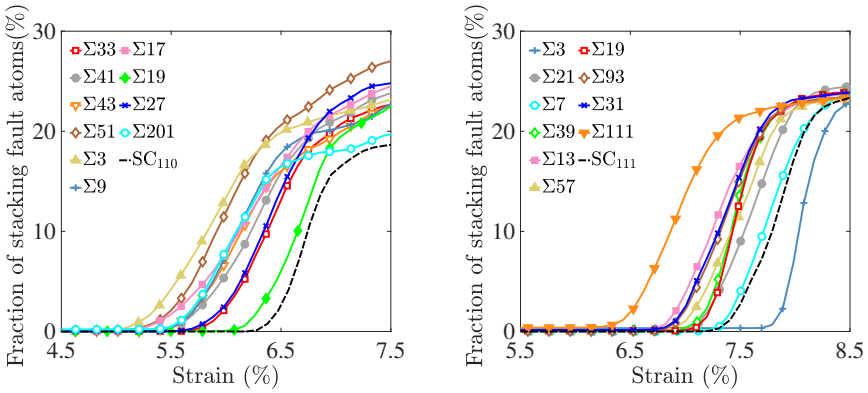

Figure 5.7: Evolution of the fraction of stacking fault atoms with respect to the total in each system as a function of tensile strain for bicrystal systems with a (a) [110] and (b) [111] loading axis. Stacking fault atoms were identified using the PTM algorithm [102].

The onset of rapid increase in the fraction of faulted atoms occurred at strains up to 30% lower than that for single crystal systems. Further, the fraction of atoms with local HCP structures (i.e., stacking faults) reaches an asymptotic value of $\approx 25\%$ at late stages of deformation. Systems with [110] STGBs nucleated partial dislocations and experienced an increase in fraction of faulted atoms at lower strain levels compared to bicrystals with [111] STBGs. The lowest levels of applied tensile strain, leading to partial dislocation nucleation and accompanying increase in the fraction of faulted atoms occurred in bicrystals with a $\Sigma 3$ [110], Fig. 5.7(b), and $\Sigma 111$ [111], Fig. 5.7(b), STGBs. Our simulation results for the evolution of the fraction of faulted atoms are qualitatively

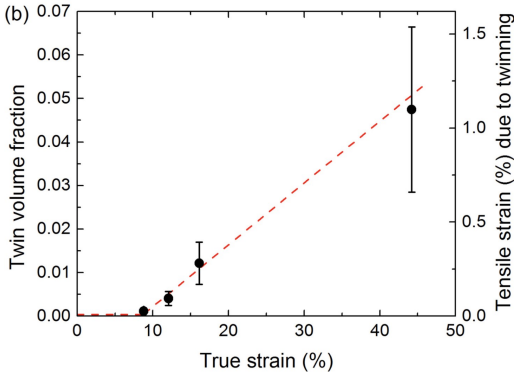

Figure 5.8: experimental result of twin volume fraction [83].

similar to recent experimental observations. Laplanche et al. [83] observed similar microstructure development as Fig. 5.7. The nucleation of deformation twins begins after a critical strain from the experiment and the volume fraction of twins monotonically increases with increasing strain [83]. To relate the trends observed in Figs. 5.2 and 5.7 to GB geometry, we obtained the ultimate stress and strain values from the peak point in the stress-strain diagram as a function of GB misorientation (i.e., twist angle) for all bicrystal systems, and the results are shown in Fig. 5.9.

Again, the bicrystal ultimate stress and strain values are lower than the single crystal ones, which is an indication that GBs in the Cantor HEA act as heterogeneous nucleation sites for dislocations. Once these dislocations nucleate from GBs, they grow by bowing into the bulk crystals leaving behind stacking faults. A close examination of Fig. 5.9 also shows that bicrystals with a [111] loading axis are characterized by higher ultimate strain [cf. Fig. 5.9(b) and Fig. 5.9(d)] and stress [cf. Fig. 5.9(a) and Fig. 5.9(c)] values, i.e., more mechanical energy is required to nucleate partial dislocations from GBs in [111] bicrystals. Variations in ultimate strain and stress values also exist as a function of GB type, defined in these bicrystal systems by the twist angle θ. For the bicrystals

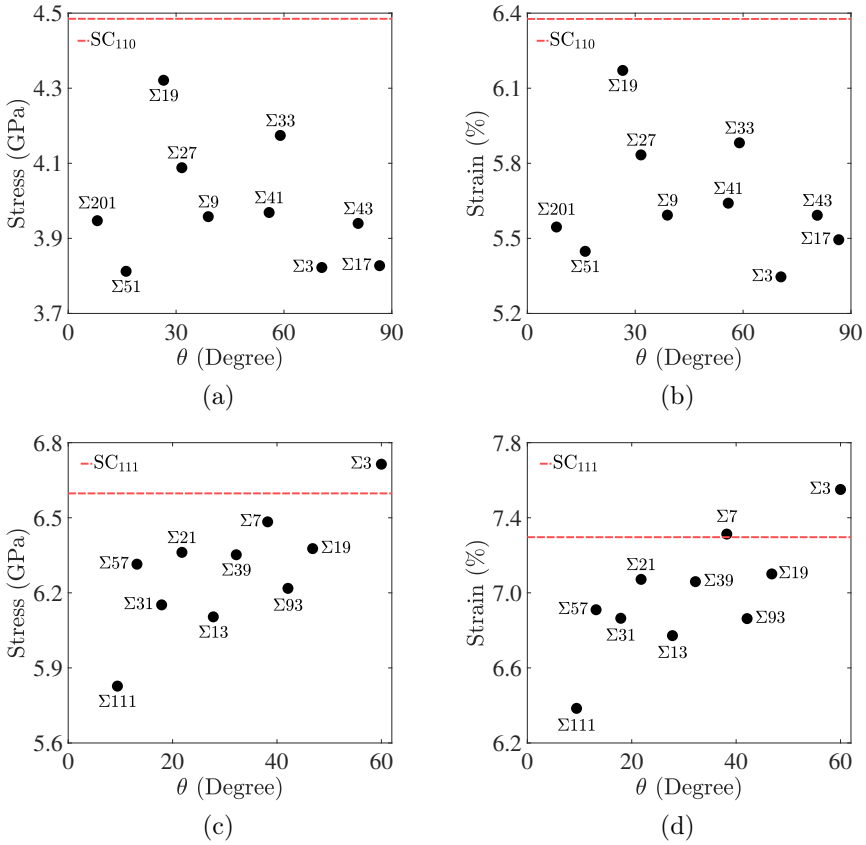

Figure 5.9: For the bicrystals with [(a)–(b)] [110] and [(c)–(d)] [111] STGBs, plots of the ultimate [(a)–(c)] stress and [(b)–(d)] strain as a function of the GBs present in these systems. Ultimate stress and strain values for Cantor alloy single crystals (dashed red lines) are also plotted for comparison.

with a [111] loading axis, a trend exists, albeit with some scatter, where the ultimate stress and strain increase with the twist angle θ. Further, an examination of Fig. 5.9(c) and (d) reveals a large difference in the nucleation stress/strain between the $\Sigma 111$ and $\Sigma 3$ GB. Owing to the small twist angle, $\theta = 9.43^{\circ}$, of $\Sigma 111$ and the well defined interfacial dislocation structure, this GB was found to be the most efficient in nucleating partial dislocations, i.e., it exhibited the smallest ultimate stress and strain values out of all [111] systems. On the other hand, dislocations were observed to nucleate homogeneously form the bulk crystals in the system with the coherent $\Sigma 3$ [111]. For the bicrystal systems with a [110] loading axis, the trends in ultimate stress and strain are not as clear as the [111] systems. Ultimate stress and strain values are lower for small ($\lesssim 30^{\circ}$) and large ($\gtrsim 60^{\circ}$) twist angles compared to intermediate ones. The [110] GBs with the twist angles of $30^{\circ} \lesssim \theta \lesssim 60^{\circ}$ displayed a scattered trend. The $\Sigma 19$ GB was the strongest, followed by $\Sigma 33$ GB and $\Sigma 27$ GB. Overall, the

results depicted in Fig. 5.9 show that while each set of [110] and [111] bicrystal systems have the same maximum Schmid factors for slip and twinning, variations do exist due to the GBs present in these systems.

5.4 Strain Rate Effects

In this section, we explore strain rate effects on the deformation behavior and stress-strain curve of the Cantor alloy. To this end, we explore the bicrystal system with a $\Sigma 111$ [111] GB. This bicrystal system was prepared following the approach detailed in Chapter 4. The engineering stress-strain curves obtained at strain rates ($4.8e{+}07 - 4.8e{+}09\ s^{-1}$) are shown in Fig. 5.10. The ultimate stress values are summarized in the Table. 5.1, which are observed to increase with increasing strain rates. The bicrystal showed about 32 % higher ultimate tensile strength at the highest strain rate ($4.8e{+}09\ s^{-1}$) compared to the lowest strain rate ($4.8e{+}07\ s^{-1}$). In addition, the flow stress after the initial stress drop for these systems approached a value of 4 GPa.

Table 5.1: Tensile properties of the bicrystal with a $\Sigma 111$ [111] GB at different strain rates

Strain rate [s^{-1}]	Ultimate tensile strength (GPa)
$4.8e{+}07$	5.49
$1.6e{+}08$	5.58
$4.8e{+}08$	5.80
$1.4e{+}09$	6.33
$4.8e{+}09$	7.33

We compared our simulation results with Cantor alloy experimental data. Shabani et al. investigated tensile behavior of CoCrFeMnNi Cantor alloy with various strain rates and found an increasing yield strength with increasing strain rate [60]. Our simulation results are in qualitative agreement with the experimental data shown in Fig. 5.11. However, the change of yield stress with the strain rate was less prominent than the simulation result. The discrepancy was attributed to the difference of the strain rate and temperature. The experimental data were acquired at the quasi-static to dynamic strain rates ($10e{-}04 - 10e{+}03\ s^{-1}$) and performed at room temperature (293 K). On the other hand, our tensile loading simulation was conducted at shock loading rates ($4.8e{+}07 - 4.8e{+}09\ s^{-1}$) with a temperature of 77 K.

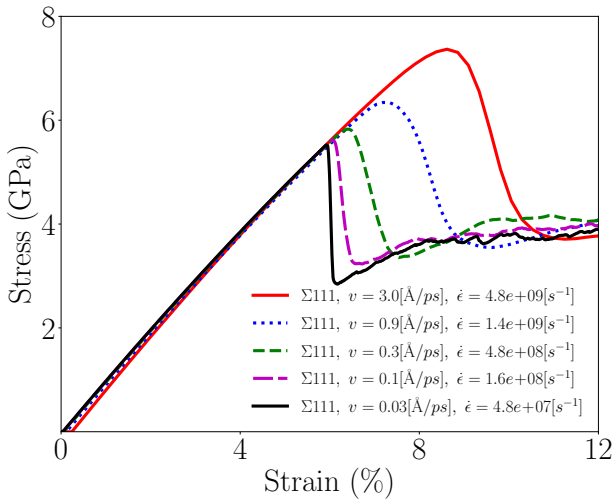

Figure 5.10: Stress–strain curves for Σ111 [111] STGB bi-crystal structures with various strain rates.

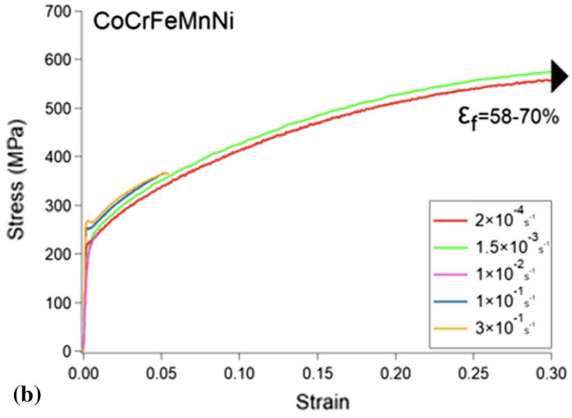

Figure 5.11: CoCrFeMnNi Cantor alloy stress-strain curves [60]

Fig. 5.12 shows snapshots of the atomic structures depicting nucleation of dislocations at the GB. The dislocation network of Σ111 are colored in yellow lines, atoms in one crystal are colored in blue, and atoms in the second crystal are removed for a better visualization of the defect structure. At the strain rate range from $4.8e{+}07$ to $1.4e{+}09$ s^{-1}, we did not observe significant variation in defect nucleation behaviors depending on the strain rate. However, we observed the simultaneous nucleation of multiple partial dislocations at the highest strain rate which is shown in Fig. 5.12 (e).

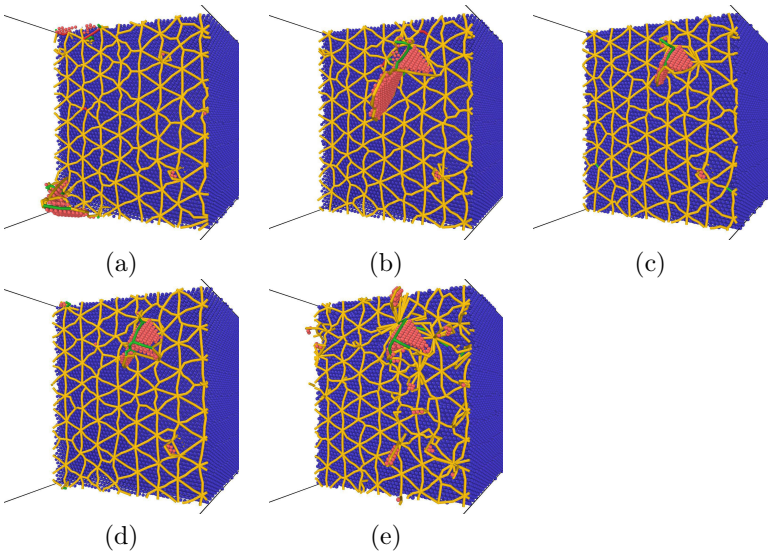

Figure 5.12: Snapshots of the Σ111 [111] STGB bicrystals with different strain rates. (a) $\dot{\epsilon} = 4.8e{+}07$ $[s^{-1}]$ with the nucleation at $\epsilon = 5.90$ % (b) $\dot{\epsilon} = 1.6e{+}08$ $[s^{-1}]$ with the nucleation at $\epsilon = 6.03$ % (c) $\dot{\epsilon} = 4.8e{+}08$ $[s^{-1}]$ with the nucleation at $\epsilon = 6.40$ % (d) $\dot{\epsilon} = 1.4e{+}09$ $[s^{-1}]$ with the nucleation at $\epsilon = 7.20$ %(e) $\dot{\epsilon} = 4.8e{+}09$ $[s^{-1}]$ with the nucleation at $\epsilon = 8.62$ %

5.5 Multiple GBs

In this section, we examined of having multiple GBs in the bicrystal system in the mechanical behavior and defect nucleation stress. To this end, we employed the Σ111 GB geometry. Several realization of this geometry, but with multiple equally-spaced GBs were constructed following the approach detailed in Chapter 4. Figure 5.13 depicts the bicrystal systems used in this study, where a total of five bicrystal geometries were constructed with one, three, five, seven, and fifteen GBs. Table 5.2 lists the dimensions of the simulation box for each system. For the tensile deformation simulations, a strain rate of $4.8e{+}08$ s^{-1} was used.

Table 5.2: Dimensions of the simulation box for the bicrystal systems with a Σ111 [111] GB with different number of GBs.

GB planes	L_x (Å)	L_y (Å)	L_z (Å)
1	104.894	586.950	121.121
3	104.894	588.607	121.121
5	104.894	590.263	121.121
7	104.894	591.919	121.121
15	104.894	598.545	121.121

The deformation behavior of the Cantor alloy bicrystals with one and 15 Σ111 STGBs is

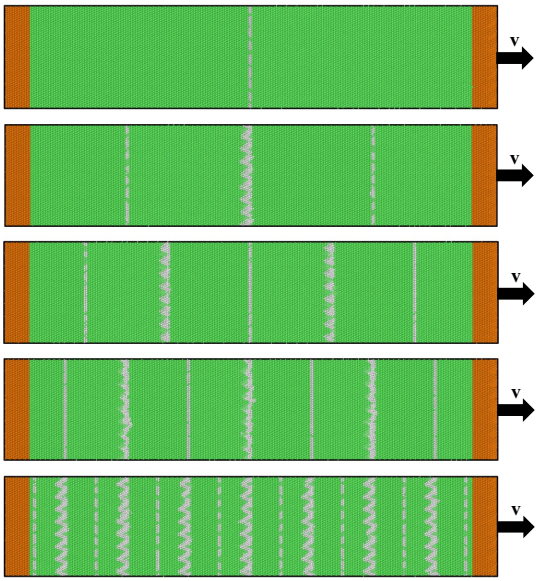

Figure 5.13: Cantor alloy bicrystals with multiple GBs. Atoms in green (white) denote FCC (GB) atoms, while atoms in orange denote rigid (left) and moving ones (right).

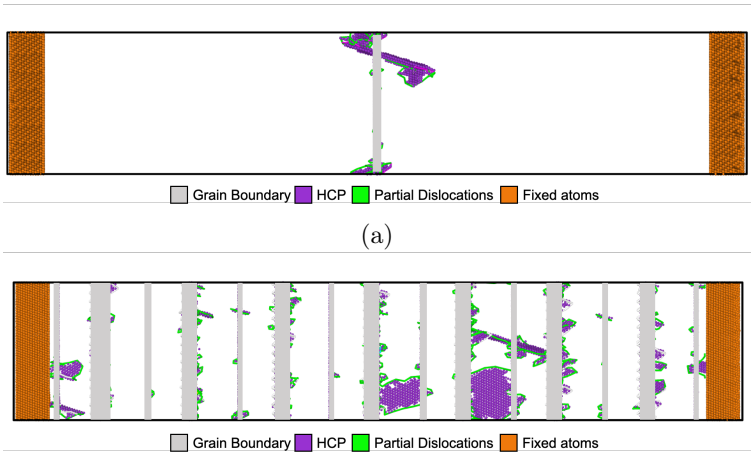

Figure 5.14: For the bicrystal system with a Σ111 GB, the onset of dislocation nucleation from the GB in a system with (a) one GB at a nominal strain of $\epsilon = 6.5$ % and (b) 15 GBs at a nominal strain of $\epsilon = 5.7$ %.

depicted in Fig. 5.14. Figure 5.14(a) shows the system with one GB at a tensile strain of $\epsilon = 6.5$ %, whereas Fig. 5.14(b) depicts the structure of the system with fifteen GBs at a tensile strain of $\epsilon = 5.7\%$. Partial dislocation lines and HCP atoms are labeled in green and purple. For a better visualization, FCC atoms are excluded from the images. It is evident that adding more GBs provided

more potential sites for defect nucleation, i.e., multiple dislocations were nucleated from the system with 15 GBs compared to one dominant dislocation in the bicrystal with one GB.

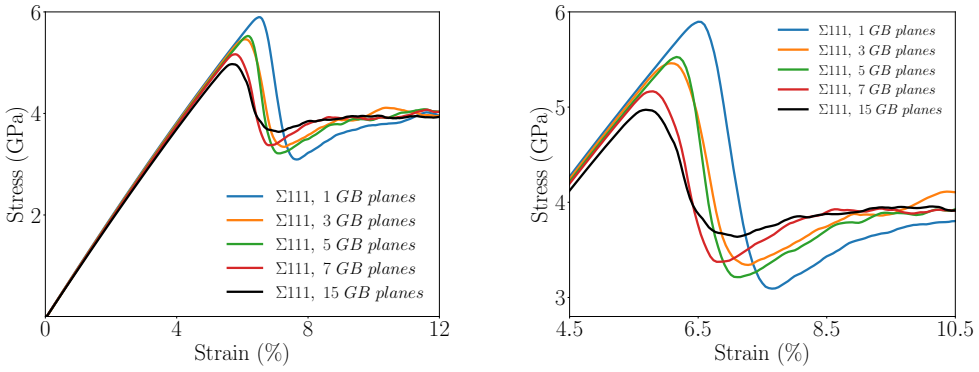

Figure 5.15: (a) Stress strain curves for the bicrystal system with a Σ111 GB with a varying number of GBs. (b) A close-up view around the peak points in the stress strain curves.

The stress strain diagram for these bicrystal systems is shown in Fig. 5.15(a) and a close-up view of the peak points in the diagrams is shown in Fig. 5.15(b). It can be seen that adding more GB planes leads to the reduction in the defect nucleation stress, i.e., peak point in the stress-strain curve shifts to lower stress. This is an indication that the addition of more GBs, all of which have the same geometry and orientation with respect to the loading axis, leads to softer bicrystal systems, where less mechanical energy is required to nucleate dislocations from these GBs. It is suggested that this is due to two main effects. First, the introduction of many GB planes increases the number of possible dislocation nucleation sites. Second, the increase in the number of GBs reduces the overall spacing between them. As a result, the interfacial dislocations that make up the Σ111 GB interact via their long-range elastic fields, which in turn affects the overall state of stress of these bicrystals.

5.6 Effect of Chemical Disorder

Due to the non-dilute nature our HEA bicrystal compositions, it is expected that variations in the ultimate stress and strain values exist due to variations in the local chemistry within GB structures. To demonstrate this effect, we examined the behavior of five realizations of the bicrystal system with Σ3 [111] STGB. Fig. 5.16(a) shows tensile stress strain curves for these systems along with that of a single crystal system with a [111] loading axis. Variations in the observed ultimate

stress and strain values are due to the local GB chemistry. Owing to the coherent nature of this Σ3 GB, it was found to be the most resistant to dislocation emission. In all systems depicted in Fig. 5.16(a), dislocations nucleated homogeneously from bulk crystals. Figure 5.16(b) depicts the structure of one bicrystal system showing the nucleation of a partial dislocation (green line) from the bulk grain, which then leaves behind a stacking fault (atoms colored in red). GB atoms are in yellow and bulk FCC atoms were removed for a better visualization of the defect structures.

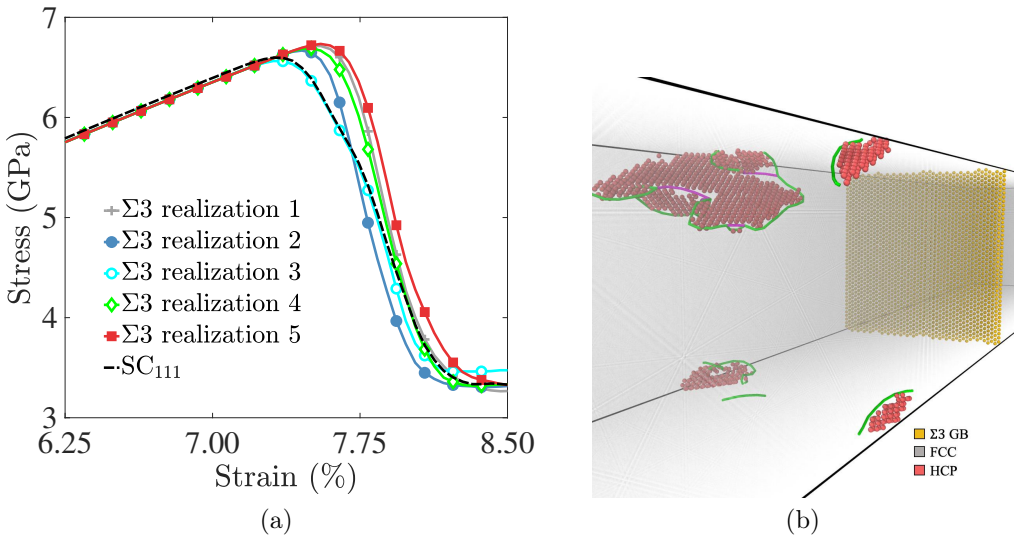

Figure 5.16: (a) Stress strain curves for five realizations of the bicrystal system with a Σ3 [111] GB, demonstrating the effect of local GB chemistry. The behavior of the single crystal with [111] loading axis is also shown for comparison. (b) Structure of one bicrystal system with a Σ3 [111] GB, showing the nucleation of a partial dislocation (green line) from the bulk crystal, which then leaves behind a stacking fault (atoms colored in red). GB atoms are in yellow and bulk FCC atoms were removed for a better visualization of the defect structures.

Chapter 6

Conclusions and Future Work

While the Cantor alloy has been the subject of numerous studies, most of these have been focused on the effects of element compositions away from the equiatomic composition [57], stacking fault energies [85, 89], and lattice distortions [37, 120, 121]. The role of GBs in the mechanical deformation of HEA alloys, therefore, remains poorly understood. Tensile stress-strain diagrams for Cantor alloy bicrystals with [110] and [111] loading axes show that GBs facilitate the nucleation of partial dislocations, which with further deformation grow in the bulk crystal leaving behind stacking faults. This is in agreement with recent experimental findings demonstrating that GBs act as nucleation sites for mechanical nanotwins [79, 83]. Due to their lower Schmid factors for twinning and slip, the bicrystals with a [111] loading axis were found to require more mechanical energy to nucleate dislocations from GBs compared to systems with a [110] loading axis. As shown in Figs. 5.4 and 5.5, nucleation of $1/6\langle 112\rangle$ dislocations in the bicrystal systems occurred at lower strain values compared to their single crystal counterparts. In addition, the local GB structure plays in role in the nucleation process. For example, the bicrystal system with a $\Sigma 111$ STGB, characterized by a grid of $1/6\langle 112\rangle$ screw dislocations [see Fig. 5.1(a)], was found to nucleate partial dislocations at the lowest strain level [refer to Fig. 5.9(c)–(d)] compared to the bicrystal systems with a [111] loading axis. Overall, our simulation results suggest that the strength of the Cantor alloy can be manipulated by tailoring the GB types and their populations in an HEA microstructure. It is worth mentioning that our approach of generating GBs in the Cantor alloy bicrystals employed the commonly used γ-surface method [108, 109], which aims to mine for the lowest energy GB structure by performing a series of relative displacements between the upper and lower crystals in conjunction with atom deletions

and energy minimizations. However, this approach does not consider chemical equilibration, which includes exploring the preferential sites within the GB for each of the elemental species, sampling the GB atomic density, and probing adsorption or desorption effects. As a result, the GB structures explored in this work can be regarded as metastable ones. Indeed, the role of GB metastability has recently received considerable attention for its influence on the behavior and properties of metallic systems [113, 122]. For future research, exploring the mechanical behavior of a larger number of GB types with different misorientation and plane normal degrees of freedom would help establish a more complete structure-property maps relating the GB geometry to the mechanical behavior of HEAs. Further, exploring GB solute segregation effects in the Cantor alloy will help researchers unravel the impact of the chemical states of GBs on the mechanical behavior of these alloys.

Appendices

Appendix A $\langle 110 \rangle$ GBs : Defect Nucleation

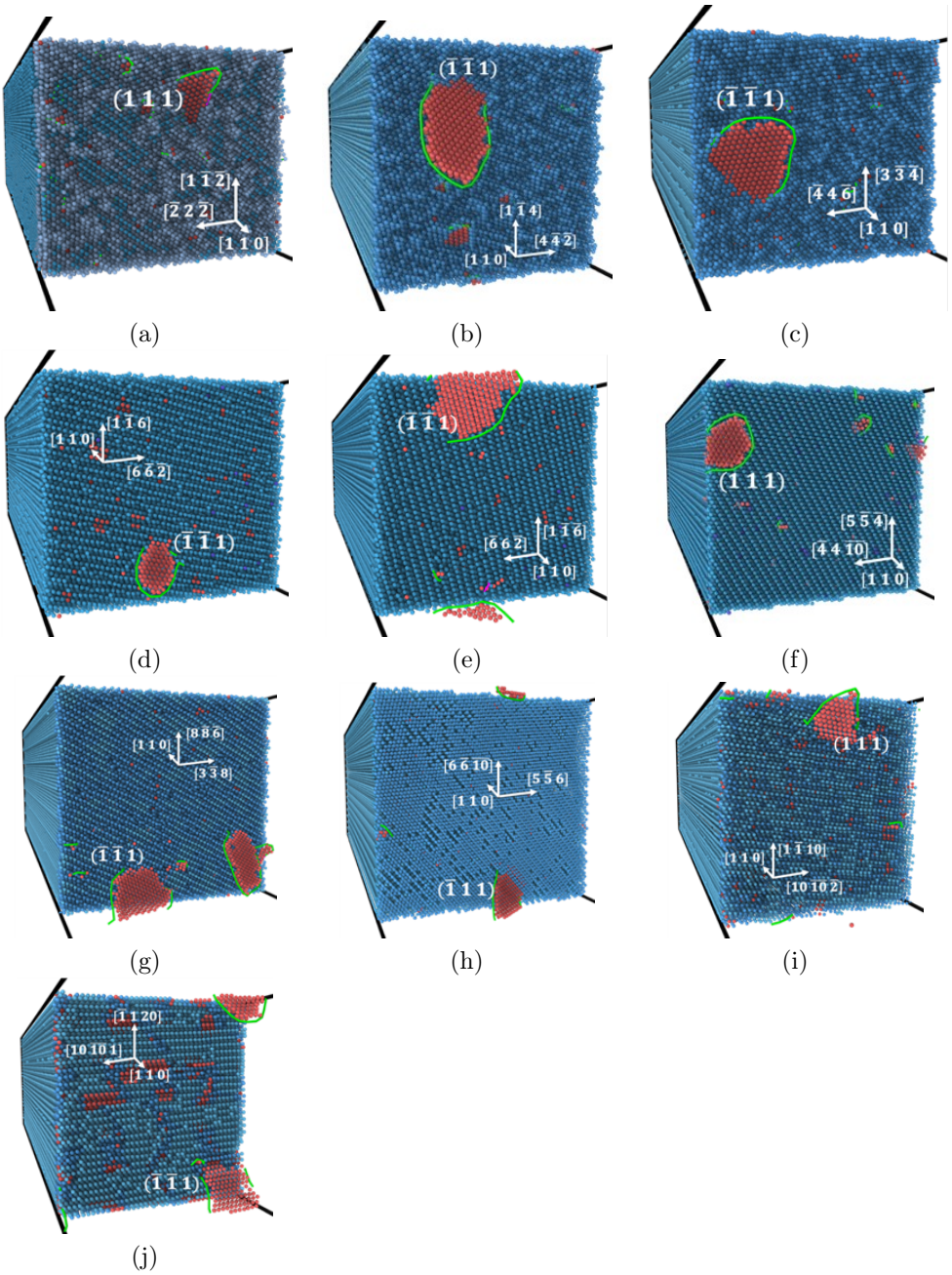

Figure 1: The FCC atoms located in either upper or lower crystal are deleted for visualization. One of crystals is chosen for deletion depending on the initial defect nucleation site. Blue spheres and red spheres represent FCC and HCP structure for each. The green lines wrap around HCP structure (stacking fault) and indicate partial dislocation lines. (a) Σ3 (b) Σ9 (c) Σ17 (d) Σ19 (e) Σ27 (f) Σ33 (g) Σ41 (h) Σ43 (i) Σ51 (j) Σ201

Appendix B $\langle 111 \rangle$ GBs : Defect Nucleation

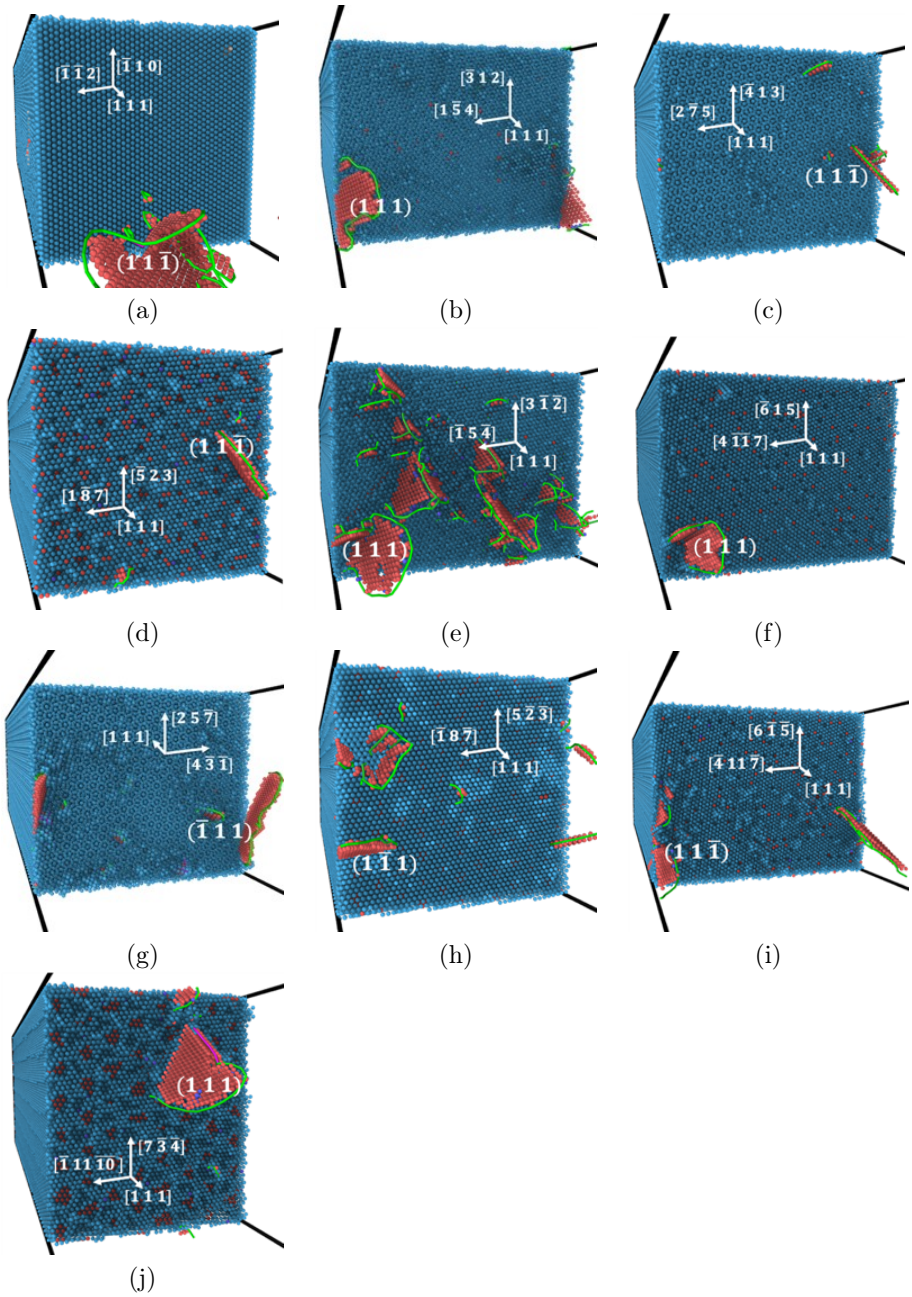

Figure 2: The FCC atoms located in either upper or lower crystal are deleted for visualization. One of crystals is chosen for deletion depending on the initial defect nucleation site. Blue spheres and red spheres represent FCC and HCP structure for each. The green lines wrap around HCP structure (stacking fault) and indicate partial dislocation lines. (a) $\Sigma 3$ (b) $\Sigma 7$ (c) $\Sigma 13$ (d) $\Sigma 19$ (e) $\Sigma 21$ (f) $\Sigma 31$ (g) $\Sigma 39$ (h) $\Sigma 57$ (i) $\Sigma 93$ (j) $\Sigma 111$

Bibliography

[1] Reza Abbaschian and Robert E Reed-Hill. *Physical metallurgy principles*. Cengage Learning, 2008.

[2] B Cantor, ITH Chang, P Knight, and AJB Vincent. Microstructural development in equiatomic multicomponent alloys. *Materials Science and Engineering: A*, 375:213–218, 2004.

[3] S. Ranganathan. Alloyed pleasures: multimetallic cocktails. *Current science*, 85(10):1404–1406, 2003.

[4] J-W Yeh, S-K Chen, S-J Lin, J-Y Gan, T-S Chin, T-T Shun, C-H Tsau, and S-Y Chang. Nanostructured high-entropy alloys with multiple principal elements: novel alloy design concepts and outcomes. *Advanced Engineering Materials*, 6(5):299–303, 2004.

[5] YJ Zhou, Y Zhang, YL Wang, and GL Chen. Solid solution alloys of $AlCoCrFeNiTi_x$ with excellent room-temperature mechanical properties. *Applied physics letters*, 90(18):181904, 2007.

[6] XF Wang, Yong Zhang, Yi Qiao, and GL Chen. Novel microstructure and properties of multicomponent $CoCrCuFeNiTi_x$ alloys. *Intermetallics*, 15(3):357–362, 2007.

[7] Che-Wei Tsai, Ming-Hung Tsai, Jien-Wei Yeh, and Chih-Chao Yang. Effect of temperature on mechanical properties of $Al_{0.5}CoCrCuFeNi$ wrought alloy. *Journal of Alloys and Compounds*, 490(1-2):160–165, 2010.

[8] Chun-Ming Lin and Hsien-Lung Tsai. Evolution of microstructure, hardness, and corrosion properties of high-entropy $Al_{0.5}CoCrFeNi$ alloy. *Intermetallics*, 19(3):288–294, 2011.

[9] Ming-Hao Chuang, Ming-Hung Tsai, Woei-Ren Wang, Su-Jien Lin, and Jien-Wei Yeh. Microstructure and wear behavior of $Al_xCo_{1.5}CrFeNi_{1.5}Ti_y$ high-entropy alloys. *Acta Materialia*, 59(16):6308–6317, 2011.

[10] Jien-Min Wu, Su-Jien Lin, Jien-Wei Yeh, Swe-Kai Chen, Yuan-Sheng Huang, and Hung-Cheng Chen. Adhesive wear behavior of $Al_xCoCrCuFeNi$ high-entropy alloys as a function of aluminum content. *Wear*, 261(5-6):513–519, 2006.

[11] YY Chen, T Duval, UD Hung, JW Yeh, and HC Shih. Microstructure and electrochemical properties of high entropy alloys—a comparison with type-304 stainless steel. *Corrosion science*, 47(9):2257–2279, 2005.

[12] Shin-Tsung Chen, Wei-Yeh Tang, Yen-Fu Kuo, Sheng-Yao Chen, Chun-Huei Tsau, Tao-Tsung Shun, and Jien-Wei Yeh. Microstructure and properties of age-hardenable $Al_xCrFe_{1.5}MnNi_{0.5}$ alloys. *Materials Science and Engineering: A*, 527(21-22):5818–5825, 2010.

[13] Yunzhu Shi, Bin Yang, and Peter K Liaw. Corrosion-resistant high-entropy alloys: a review. *Metals*, 7(2):43, 2017.

[14] H Torbati-Sarraf, Mitra Shabani, Paul D Jablonski, Garrett J Pataky, and A Poursaee. The influence of incorporation of mn on the pitting corrosion performance of crfeconi high entropy alloy at different temperatures. *Materials & Design*, 184:108170, 2019.

[15] David A Porter and Kenneth E Easterling. *Phase transformations in metals and alloys (revised reprint)*. CRC press, 2009.

[16] Jien-Wei Yeh. Recent progress in high entropy alloys. *Annales de Chimie Science des Matériaux*, 31(6):633–648, 2006.

[17] Jien-Wei Yeh. Alloy design strategies and future trends in high-entropy alloys. *JOM*, 65(12): 1759–1771, 2013.

[18] Michael C Gao, Jien-Wei Yeh, Peter K Liaw, Yong Zhang, et al. High-entropy alloys. *Cham: Springer International Publishing*, 2016.

[19] YF Ye, Q Wang, J Lu, CT Liu, and Yon Yang. High-entropy alloy: challenges and prospects. *Materials Today*, 19(6):349–362, 2016.

[20] Easo P George, Dierk Raabe, and Robert O Ritchie. High-entropy alloys. *Nature Reviews Materials*, 4(8):515–534, 2019.

[21] Chung-Jin Tong, Yu-Liang Chen, Jien-Wei Yeh, Su-Jien Lin, Swe-Kai Chen, Tao-Tsung Shun, Chun-Huei Tsau, and Shou-Yi Chang. Microstructure characterization of al x cocrcufeni high-entropy alloy system with multiprincipal elements. *Metallurgical and Materials Transactions A*, 36(4):881–893, 2005.

[22] A Manzoni, H Daoud, R Völkl, U Glatzel, and N Wanderka. Phase separation in equiatomic AlCoCrFeNi high-entropy alloy. *Ultramicroscopy*, 132:212–215, 2013.

[23] Yao-Jian Liang, Linjing Wang, Yuren Wen, Baoyuan Cheng, Qinli Wu, Tangqing Cao, Qian Xiao, Yunfei Xue, Gang Sha, Yandong Wang, et al. High-content ductile coherent nanoprecipitates achieve ultrastrong high-entropy alloys. *Nature communications*, 9(1):1–8, 2018.

[24] James A Hanna, Ian Baker, Markus W Wittmann, and Paul R Munroe. A new high-strength spinodal alloy. *Journal of materials research*, 20(4):791–795, 2005.

[25] Louis J Santodonato, Yang Zhang, Mikhail Feygenson, Chad M Parish, Michael C Gao, Richard JK Weber, Joerg C Neuefeind, Zhi Tang, and Peter K Liaw. Deviation from high-entropy configurations in the atomic distributions of a multi-principal-element alloy. *Nature communications*, 6(1):1–13, 2015.

[26] Woong Kil Choo, JH Kim, and JC Yoon. Microstructural change in austenitic Fe-30.0 wt% Mn-7.8 wt% Al-1.3 wt% Cinitiated by spinodal decomposition and its influence on mechanical properties. *Acta Materialia*, 45(12):4877–4885, 1997.

[27] Jogender Singh and CM Wayman. Age-hardening characteristics of a martensitic FeNiMn alloy. *Materials Science and Engineering*, 94:233–242, 1987.

[28] F Zhu, P Haasen, and R Wagner. An atom probe study of the decomposition of FeCrCo permanent magnet alloys. *Acta Metallurgica*, 34(3):457–463, 1986.

[29] MK Miller, JM Hyde, MG Hetherington, A Cerezo, GDW Smith, and CM Elliott. Spinodal decomposition in Fe-Cr alloys: Experimental study at the atomic level and comparison with computer models—i. introduction and methodology. *Acta Metallurgica et Materialia*, 43(9): 3385–3401, 1995.

[30] V Soni, ON Senkov, B Gwalani, DB Miracle, and Rajarshi Banerjee. Microstructural design for improving ductility of an initially brittle refractory high entropy alloy. *Scientific reports*, 8 (1):1–10, 2018.

[31] LB Chen, R Wei, K Tang, J Zhang, F Jiang, and J Sun. Ductile-brittle transition of carbon alloyed $Fe_{40}Mn_{40}Co_{10}Cr_{10}$ high entropy alloys. *Materials Letters*, 236:416–419, 2019.

[32] T Yang, YL Zhao, WH Liu, JH Zhu, JJ Kai, and CT Liu. Ductilizing brittle high-entropy alloys via tailoring valence electron concentrations of precipitates by controlled elemental partitioning. *Materials Research Letters*, 6(10):600–606, 2018.

[33] Zhijun Wang, Weifeng Qiu, Yong Yang, and CT Liu. Atomic-size and lattice-distortion effects in newly developed high-entropy alloys with multiple principal elements. *Intermetallics*, 64: 63–69, 2015.

[34] Jien-Wei Yeh, Su-Jien Lin, Tsung-Shune Chin, Jon-Yiew Gan, Swe-Kai Chen, Tao-Tsung Shun, Chung-Huei Tsau, and Shou-Yi Chou. Formation of simple crystal structures in cu-co-ni-cr-al-fe-ti-v alloys with multiprincipal metallic elements. *Metallurgical and Materials Transactions A Volume 35*, (8):2533–2536, 2004.

[35] BS Murty, JW Yeh, and S Ranganathan. High-entropy alloys. 2014.

[36] Jien-Wei Yeh, Shou-Yi Chang, Yu-Der Hong, Swe-Kai Chen, and Su-Jien Lin. Anomalous decrease in x-ray diffraction intensities of Cu–Ni–Al–Co–Cr–Fe–Si alloy systems with multi-principal elements. *Materials chemistry and physics*, 103(1):41–46, 2007.

[37] Peng Wang, Yuan Wu, Jiabin Liu, and Hongtao Wang. Impacts of atomic scale lattice distortion on dislocation activity in high-entropy alloys. *Extreme Mechanics Letters*, 17:38–42, 2017.

[38] Li Li, Qihong Fang, Jia Li, Bin Liu, Yong Liu, and Peter K Liaw. Lattice-distortion dependent yield strength in high entropy alloys. *Materials Science and Engineering: A*, page 139323, 2020.

[39] YY Zhao and TG Nieh. Correlation between lattice distortion and friction stress in ni-based equiatomic alloys. *Intermetallics*, 86:45–50, 2017.

[40] Hui-Wen Chang, Ping-Kang Huang, Jien-Wei Yeh, Andrew Davison, Chun-Huei Tsau, and Chih-Chao Yang. Influence of substrate bias, deposition temperature and post-deposition annealing on the structure and properties of multi-principal-component (alcrmositi) n coatings. *Surface and Coatings Technology*, 202(14):3360–3366, 2008.

[41] Daniel B Miracle and Oleg N Senkov. A critical review of high entropy alloys and related concepts. *Acta Materialia*, 122:448–511, 2017.

[42] Sheela Singh, Nelia Wanderka, BS Murty, Uwe Glatzel, and John Banhart. Decomposition in multi-component AlCoCrCuFeNi high-entropy alloy. *Acta Materialia*, 59(1):182–190, 2011.

[43] C Li, JC Li, M Zhao, and Q Jiang. Effect of alloying elements on microstructure and properties of multiprincipal elements high-entropy alloys. *Journal of Alloys and Compounds*, 475(1-2): 752–757, 2009.

[44] K Zhao, XX Xia, HY Bai, DQ Zhao, and WH Wang. Room temperature homogeneous flow in a bulk metallic glass with low glass transition temperature. *Applied Physics Letters*, 98(14): 141913, 2011.

[45] Li Lu. *Advanced Materials and Processing 2010: Proceedings of the 6th International Conference on ICAMP, Yunnan, PR China, 19-23 July 2010*. world scientific, 2011.

[46] Yong Zhang, Ting Ting Zuo, Zhi Tang, Michael C Gao, Karin A Dahmen, Peter K Liaw, and Zhao Ping Lu. Microstructures and properties of high-entropy alloys. *Progress in Materials Science*, 61:1–93, 2014.

[47] Zhenggang Wu, Hongbin Bei, Frederik Otto, George Mathews Pharr, and Easo P George. Recovery, recrystallization, grain growth and phase stability of a family of fcc-structured multi-component equiatomic solid solution alloys. *Intermetallics*, 46:131–140, 2014.

[48] Bernd Gludovatz, Anton Hohenwarter, Dhiraj Catoor, Edwin H Chang, Easo P George, and Robert O Ritchie. A fracture-resistant high-entropy alloy for cryogenic applications. *Science*, 345(6201):1153–1158, 2014.

[49] Yuan Wu, WH Liu, XL Wang, Dong Ma, Alexandru Dan Stoica, TG Nieh, ZB He, and ZP Lu. In-situ neutron diffraction study of deformation behavior of a multi-component high-entropy alloy. *Applied Physics Letters*, 104(5):051910, 2014.

[50] MS Lucas, GB Wilks, L Mauger, Jorge A Munoz, Oleg N Senkov, E Michel, J Horwath, SL Semiatin, Matthew B Stone, Douglas L Abernathy, et al. Absence of long-range chemical ordering in equimolar fecocrni. *Applied Physics Letters*, 100(25):251907, 2012.

[51] MJ Yao, Konda Gokuldoss Pradeep, Cemal Cem Tasan, and Dierk Raabe. A novel, single phase, non-equiatomic FeMnNiCoCr high-entropy alloy with exceptional phase stability and tensile ductility. *Scripta Materialia*, 72:5–8, 2014.

[52] Frederik Otto, A Dlouhỳ, Ch Somsen, Hongbin Bei, G Eggeler, and Easo P George. The influences of temperature and microstructure on the tensile properties of a cocrfemnni high-entropy alloy. *Acta Materialia*, 61(15):5743–5755, 2013.

[53] Bernd Gludovatz, Anton Hohenwarter, Keli VS Thurston, Hongbin Bei, Zhenggang Wu, Easo P George, and Robert O Ritchie. Exceptional damage-tolerance of a medium-entropy alloy crconi at cryogenic temperatures. *Nature communications*, 7(1):1–8, 2016.

[54] Joseph J Licavoli, Michael C Gao, John S Sears, Paul D Jablonski, and Jeffrey A Hawk. Microstructure and mechanical behavior of high-entropy alloys. *Journal of Materials Engineering and Performance*, 24(10):3685–3698, 2015.

[55] SW Wu, G Wang, J Yi, YD Jia, I Hussain, QJ Zhai, and PK Liaw. Strong grain-size effect on deformation twinning of an al0. 1cocrfeni high-entropy alloy. *Materials Research Letters*, 5 (4):276–283, 2017.

[56] SJ Sun, YZ Tian, HR Lin, HJ Yang, XG Dong, YH Wang, and ZF Zhang. Transition of twinning behavior in cocrfemnni high entropy alloy with grain refinement. *Materials Science and Engineering: A*, 712:603–607, 2018.

[57] Won-Mi Choi, Yong Hee Jo, Seok Su Sohn, Sunghak Lee, and Byeong-Joo Lee. Understanding the physical metallurgy of the CoCrFeMnNi high-entropy alloy: an atomistic simulation study. *npj Computational Materials*, 4(1):1–9, 2018.

[58] Zhiming Li, Konda Gokuldoss Pradeep, Yun Deng, Dierk Raabe, and Cemal Cem Tasan. Metastable high-entropy dual-phase alloys overcome the strength–ductility trade-off. *Nature*, 534(7606):227–230, 2016.

[59] Evan Ma and Xiaolei Wu. Tailoring heterogeneities in high-entropy alloys to promote strength–ductility synergy. *Nature Communications*, 10(1):1–10, 2019.

[60] Mitra Shabani, Joseph Indeck, Kavan Hazeli, Paul D Jablonski, and Garrett J Pataky. Effect of strain rate on the tensile behavior of cocrfeni and cocrfemnni high-entropy alloys. *Journal of Materials Engineering and Performance*, 28(7):4348–4356, 2019.

[61] Yun Deng, Cemal Cem Tasan, Konda Gokuldoss Pradeep, Hauke Springer, Aleksander Kostka, and Dierk Raabe. Design of a twinning-induced plasticity high entropy alloy. *Acta Materialia*, 94:124–133, 2015.

[62] Cameron L Tracy, Sulgiye Park, Dylan R Rittman, Steven J Zinkle, Hongbin Bei, Maik Lang, Rodney C Ewing, and Wendy L Mao. High pressure synthesis of a hexagonal close-packed phase of the high-entropy alloy CrMnFeCoNi. *Nature communications*, 8(1):1–6, 2017.

[63] Fei Zhang, Yuan Wu, Hongbo Lou, Zhidan Zeng, Vitali B Prakapenka, Eran Greenberg, Yang Ren, Jinyuan Yan, John S Okasinski, Xiongjun Liu, et al. Polymorphism in a high-entropy alloy. *Nature communications*, 8(1):1–7, 2017.

[64] Stéphane Gorsse, Daniel B Miracle, and Oleg N Senkov. Mapping the world of complex concentrated alloys. *Acta Materialia*, 135:177–187, 2017.

[65] Amanda Haglund, Michael Koehler, Dhiraj Catoor, Easo P George, and Veerle Keppens. Polycrystalline elastic moduli of a high-entropy alloy at cryogenic temperatures. *Intermetallics*, 58:62–64, 2015.

[66] G Laplanche, P Gadaud, O Horst, F Otto, G Eggeler, and EP George. Temperature dependencies of the elastic moduli and thermal expansion coefficient of an equiatomic, single-phase CoCrFeMnNi high-entropy alloy. *Journal of Alloys and Compounds*, 623:348–353, 2015.

[67] Fuyang Tian, Lajos Károly Varga, Jiang Shen, and Levente Vitos. Calculating elastic constants in high-entropy alloys using the coherent potential approximation: Current issues and errors. *Computational materials science*, 111:350–358, 2016.

[68] HY Diao, R Feng, Karin A Dahmen, and PK Liaw. Fundamental deformation behavior in high-entropy alloys: An overview. *Current Opinion in Solid State and Materials Science*, 21 (5):252–266, 2017.

[69] Frederik Otto, Ying Yang, Hongbin Bei, and Easo P George. Relative effects of enthalpy and entropy on the phase stability of equiatomic high-entropy alloys. *Acta Materialia*, 61(7): 2628–2638, 2013.

[70] Aravind Gali and Easo P George. Tensile properties of high-and medium-entropy alloys. *Intermetallics*, 39:74–78, 2013.

[71] PP Bhattacharjee, GD Sathiaraj, M Zaid, JR Gatti, Chi Lee, Che-Wei Tsai, and Jien-Wei Yeh. Microstructure and texture evolution during annealing of equiatomic cocrfemnni high-entropy alloy. *Journal of Alloys and Compounds*, 587:544–552, 2014.

[72] GA Salishchev, MA Tikhonovsky, DG Shaysultanov, ND Stepanov, AV Kuznetsov, IV Kolodiy, AS Tortika, and ON Senkov. Effect of mn and v on structure and mechanical properties of high-entropy alloys based on cocrfeni system. *Journal of Alloys and Compounds*, 591:11–21, 2014.

[73] ND Stepanov, DG Shaysultanov, N Yu Yurchenko, SV Zherebtsov, AN Ladygin, GA Salishchev, and MA Tikhonovsky. High temperature deformation behavior and dynamic recrystallization in cocrfenimn high entropy alloy. *Materials Science and Engineering: A*, 636: 188–195, 2015.

[74] Frederik Otto, Antonín Dlouhỳ, Konda Gokuldoss Pradeep, Monika Kuběnová, Dierk Raabe, G Eggeler, and Easo P George. Decomposition of the single-phase high-entropy alloy crmnfeconi after prolonged anneals at intermediate temperatures. *Acta Materialia*, 112:40–52, 2016.

[75] Frederik Otto, Nikki L Hanold, and Easo P George. Microstructural evolution after thermomechanical processing in an equiatomic, single-phase cocrfemnni high-entropy alloy with special focus on twin boundaries. *Intermetallics*, 54:39–48, 2014.

[76] G Laplanche, O Horst, F Otto, G Eggeler, and EP George. Microstructural evolution of a cocrfemnni high-entropy alloy after swaging and annealing. *Journal of Alloys and Compounds*, 647:548–557, 2015.

[77] B Schuh, F Mendez-Martin, B Völker, Easo P George, Helmut Clemens, R Pippan, and Anton Hohenwarter. Mechanical properties, microstructure and thermal stability of a nanocrystalline CoCrFeMnNi high-entropy alloy after severe plastic deformation. *Acta Materialia*, 96:258–268, 2015.

[78] Mathilde Laurent-Brocq, Alfiya Akhatova, Loïc Perrière, Siham Chebini, Xavier Sauvage, Eric Leroy, and Yannick Champion. Insights into the phase diagram of the crmnfeconi high entropy alloy. *Acta Materialia*, 88:355–365, 2015.

[79] S-H Joo, H Kato, MJ Jang, J Moon, CW Tsai, JW Yeh, and HS Kim. Tensile deformation behavior and deformation twinning of an equimolar cocrfemnni high-entropy alloy. *Materials Science and Engineering: A*, 689:122–133, 2017.

[80] Bingfeng Wang, Ao Fu, Xiaoxia Huang, Bin Liu, Yong Liu, Zezhou Li, and Xiang Zan. Mechanical properties and microstructure of the cocrfemnni high entropy alloy under high strain rate compression. *Journal of Materials Engineering and Performance*, 25(7):2985–2992, 2016.

[81] JY He, WH Liu, H Wang, Y Wu, XJ Liu, TG Nieh, and ZP Lu. Effects of al addition on structural evolution and tensile properties of the feconicrmn high-entropy alloy system. *Acta Materialia*, 62:105–113, 2014.

[82] Zhenggang Wu, Hongbin Bei, George M Pharr, and Easo P George. Temperature dependence of the mechanical properties of equiatomic solid solution alloys with face-centered cubic crystal structures. *Acta Materialia*, 81:428–441, 2014.

[83] G Laplanche, A Kostka, OM Horst, G Eggeler, and EP George. Microstructure evolution and critical stress for twinning in the crmnfeconi high-entropy alloy. *Acta Materialia*, 118:152–163, 2016.

[84] EJ Pickering and NG Jones. High-entropy alloys: a critical assessment of their founding principles and future prospects. *International Materials Reviews*, 61(3):183–202, 2016.

[85] Norihiko L Okamoto, Shu Fujimoto, Yuki Kambara, Marino Kawamura, Zhenghao MT Chen, Hirotaka Matsunoshita, Katsushi Tanaka, Haruyuki Inui, and Easo P George. Size effect, critical resolved shear stress, stacking fault energy, and solid solution strengthening in the crmnfeconi high-entropy alloy. *Scientific reports*, 6:35863, 2016.

[86] N Stepanov, M Tikhonovsky, N Yurchenko, D Zyabkin, M Klimova, S Zherebtsov, A Efimov, and G Salishchev. Effect of cryo-deformation on structure and properties of CoCrFeNiMn high-entropy alloy. *Intermetallics*, 59:8–17, 2015.

[87] George Ellwood Dieter and David J Bacon. *Mechanical metallurgy*, volume 3. McGraw-hill New York, 1986.

[88] AJ Zaddach, C Niu, CC Koch, and DL Irving. Mechanical properties and stacking fault energies of nifecrcomn high-entropy alloy. *JOM*, 65(12):1780–1789, 2013.

[89] Shuo Huang, Wei Li, Song Lu, Fuyang Tian, Jiang Shen, Erik Holmström, and Levente Vitos. Temperature dependent stacking fault energy of FeCrCoNiMn high entropy alloy. *Scripta Materialia*, 108:44–47, 2015.

[90] Qingqing Ding, Xiaoqian Fu, Dengke Chen, Hongbin Bei, Bernd Gludovatz, Jixue Li, Ze Zhang, Easo P George, Qian Yu, Ting Zhu, et al. Real-time nanoscale observation of deformation mechanisms in crconi-based medium-to high-entropy alloys at cryogenic temperatures. *Materials Today*, 25:21–27, 2019.

[91] Re L Bell and Robert Wolfgang Cahn. The dynamics of twinning and the interrelation of slip and twinning in zinc crystals. *Proceedings of the Royal Society of London. Series A. Mathematical and Physical Sciences*, 239(1219):494–521, 1957.

[92] RL Bell and RW Cahn. The nucleation problem in deformation twinning. *Acta Metallurgica*, 1(6):752–753, 1953.

[93] J Wang, IJ Beyerlein, and JP Hirth. Nucleation of elementary and twinning dislocations at a twin boundary in hexagonal close-packed crystals. *Modelling and Simulation in Materials Science and Engineering*, 20(2):024001, 2012.

[94] Peter Molnár, Aleš Jäger, and Pavel Lejček. Twin nucleation at grain boundaries in mg–3 wt.% al–1 wt.% zn alloy processed by equal channel angular pressing. *Scripta Materialia*, 67 (5):467–470, 2012.

[95] L Wang, P Eisenlohr, Y Yang, TR Bieler, and MA Crimp. Nucleation of paired twins at grain boundaries in titanium. *Scripta Materialia*, 63(8):827–830, 2010.

[96] Zhe Jin and Thomas R Bieler. An in-situ observation of mechanical twin nucleation and propagation in tial. *Philosophical Magazine A*, 71(5):925–947, 1995.

[97] Pavel Lejcek. *Grain boundary segregation in metals*, volume 136. Springer Science & Business Media, 2010.

[98] T Fujiwara, E Tatumoto, and T Hirokawa. This journal 11 (1942), 311. T. Fujiwara and T. Yamashita; This Journal 12 (1942), 163. E. Tatsumoto; This journal 12 (1942), 173. ML Kronberg and FH Wilson. *Trans. AIME*, 185:501, 1949.

[99] Steve Plimpton. Fast parallel algorithms for short-range molecular dynamics. *J. Comp. Phys.*, 117(1):1 – 19, 1995. doi: https://doi.org/10.1006/jcph.1995.1039.

[100] Alexander Stukowski. Visualization and analysis of atomistic simulation data with ovito, the open visualization tool. *Mod and Sim and Mater and Sci and Eng*, 18(1):015012, 2010.

[101] Alexander Stukowski, Vasily V Bulatov, and Athanasios Arsenlis. Automated identification and indexing of dislocations in crystal interfaces. *Modelling and Simulation in Materials Science and Engineering*, 20(8):085007, 2012.

[102] Peter Mahler Larsen, Søren Schmidt, and Jakob Schiøtz. Robust structural identification via polyhedral template matching. *Modelling and Simulation in Materials Science and Engineering*, 24(5):055007, 2016.

[103] Wataru Shinoda, Motoyuki Shiga, and Masuhiro Mikami. Rapid estimation of elastic constants by molecular dynamics simulation under constant stress. *Physical Review B*, 69(13):134103, 2004.

[104] Hao Jiang and Izabela Szlufarska. Small-angle twist grain boundaries as sinks for point defects. *Scientific reports*, 8(1):1–13, 2018.

[105] Qing Yin, Zhiqiang Wang, Rajiv Mishra, and Zhenhai Xia. Atomic simulations of twist grain boundary structures and deformation behaviors in aluminum. *AIP Advances*, 7(1):015040, 2017.

[106] Bo-Ru Chen, An-Chou Yeh, and Jien-Wei Yeh. Effect of one-step recrystallization on the grain boundary evolution of CoCrFeMnNi high entropy alloy and its subsystems. *Scientific reports*, 6:22306, 2016.

[107] Qingyun Lin, Xianghai An, Hongwei Liu, Qunhua Tang, Pinqiang Dai, and Xiaozhou Liao. In-situ high-resolution transmission electron microscopy investigation of grain boundary dislocation activities in a nanocrystalline CrMnFeCoNi high-entropy alloy. *Journal of Alloys and Compounds*, 709:802–807, 2017.

[108] Yuri Mishin and Diana Farkas. Atomistic simulation of [001] symmetrical tilt grain boundaries in NiAl. *Philosophical Magazine A*, 78(1):29–56, 1998.

[109] A Suzuki and Yu Mishin. Atomistic modeling of point defects and diffusion in copper grain boundaries. *Interface science*, 11(1):131–148, 2003.

[110] Timofey Frolov, Wahyu Setyawan, RJ Kurtz, Jaime Marian, Artem R Oganov, Robert E Rudd, and Qiang Zhu. Grain boundary phases in bcc metals. *Nanoscale*, 10(17):8253–8268, 2018.

[111] Qiang Zhu, Amit Samanta, Bingxi Li, Robert E Rudd, and Timofey Frolov. Predicting phase behavior of grain boundaries with evolutionary search and machine learning. *Nature communications*, 9(1):1–9, 2018.

[112] Paul Wynblatt and Dominique Chatain. Modeling grain boundary and surface segregation in multicomponent high-entropy alloys. *Physical Review Materials*, 3(5):054004, 2019.

[113] T Frolov, SV Divinski, M Asta, and Y Mishin. Effect of interface phase transformations on diffusion and segregation in high-angle grain boundaries. *Physical review letters*, 110(25): 255502, 2013.

[114] Jian Han, Vaclav Vitek, and David J Srolovitz. Grain-boundary metastability and its statistical properties. *Acta Materialia*, 104:259–273, 2016.

[115] IV Kireeva, Yu I Chumlyakov, ZV Pobedennaya, IV Kuksgausen, and I Karaman. Orientation dependence of twinning in single crystalline CoCrFeMnNi high-entropy alloy. *Materials Science and Engineering: A*, 705:176–181, 2017.

[116] Liang Zhang, Cheng Lu, and Kiet Tieu. Atomistic simulation of tensile deformation behavior of $\Sigma 5$ tilt grain boundaries in copper bicrystal. *Scientific reports*, 4:5919, 2014.

[117] Douglas E Spearot, Mark A Tschopp, Karl I Jacob, and David L McDowell. Tensile strength of$<1\,0\,0>$ and$<1\,1\,0>$ tilt bicrystal copper interfaces. *Acta materialia*, 55(2):705–714, 2007.

[118] L Capolungo, DE Spearot, M Cherkaoui, DL McDowell, J Qu, and KI Jacob. Dislocation nucleation from bicrystal interfaces and grain boundary ledges: Relationship to nanocrystalline deformation. *Journal of the Mechanics and Physics of Solids*, 55(11):2300–2327, 2007.

[119] PM Derlet and H Van Swygenhoven. Length scale effects in the simulation of deformation properties of nanocrystalline metals. *Scripta Materialia*, 47(11):719–724, 2002.

[120] Hyun Seok Oh, Duancheng Ma, Gerard Paul Leyson, Blazej Grabowski, Eun Soo Park, Fritz Körmann, and Dierk Raabe. Lattice distortions in the FeCoNiCrMn high entropy alloy studied by theory and experiment. *Entropy*, 18(9):321, 2016.

[121] YF Ye, YH Zhang, QF He, Y Zhuang, S Wang, SQ Shi, A Hu, J Fan, and Y Yang. Atomic-scale distorted lattice in chemically disordered equimolar complex alloys. *Acta Materialia*, 150: 182–194, 2018.

[122] J Chen and SJ Fensin. Associating damage nucleation and distribution with grain boundary characteristics in Ta. *Scripta Materialia*, 187:329–334, 2020.